

1 **Large iron isotope variation in the eastern Pacific mantle as a**
2 **consequence of ancient low-degree melt metasomatism**

3 Pu Sun^{1,2*}, Yaoling Niu^{2,3,4**}, Pengyuan Guo^{1,2}, Meng Duan^{1,2}, Shuo Chen^{1,2},
4 Hongmei Gong^{1,2}, Xiaohong Wang^{1,2}, Yuanyuan Xiao^{1,2}

5 ¹ Key Laboratory of Marine Geology and Environment, Institute of Oceanology, Chinese Academy of
6 Sciences, Qingdao 266071, China.

7 ² Laboratory for Marine Geology, Qingdao National Laboratory for Marine Science and Technology,
8 Qingdao 266061, China.

9 ³ Department of Earth Sciences, Durham University, Durham DH1 3LE, UK.

10 ⁴ School of Earth Science and Resources, China University of Geosciences, Beijing 100083, China.

11 Correspondence authors at:

12 Dr. Pu Sun*: Institute of Oceanology, Chinese Academy of Sciences, Qingdao 266071, China.

13 *E-mail address:* pu.sun@qdio.ac.cn

14 Dr. Yaoling Niu**: Department of Earth Sciences, Durham University, Durham DH1 3LE, UK.

15 *E-mail address:* yaoling.niu@durham.ac.uk

16

17 **Abstract**

18 Studies of mid-ocean ridge basalts (MORB) have revealed a heterogeneous
19 asthenospheric mantle in chemical elements and radiogenic isotopes. Here we report
20 that MORB mantle is also heterogeneous in Fe isotopes through studying the glass
21 samples from seamounts flanking the northern East Pacific Rise between 15° and 15°N.
22 These samples show large Fe isotope variation with $\delta^{56}\text{Fe}$ values (+ 0.03‰ to +
23 0.36‰) exceeding the known range of MORB (+ 0.05‰ to + 0.17‰). Such highly
24 varied $\delta^{56}\text{Fe}$ values cannot be well explained by seafloor alteration, fractional
25 crystallization or partial melting processes, but instead require a source mantle
26 significantly heterogeneous in Fe isotope compositions. Importantly, the $\delta^{56}\text{Fe}$ values
27 of these basalts correlate significantly with major and trace elements and Sr-Nd-Pb-Hf
28 radiogenic isotopes, reflecting melting-induced mixing of a two-component mantle
29 with the enriched component having heavy Fe isotope compositions dispersed as
30 physically distinct domains in the depleted mantle matrix. The major and trace
31 element characteristics of the enriched mantle component, as inferred from these
32 basalts, are consistent with a low-degree melting origin. Such low-degree melts with
33 heavy Fe isotope compositions most likely formed at sites such as the
34 lithosphere-asthenosphere boundary beneath ocean basins, which can metasomatize
35 the overlying oceanic lithosphere by crystallizing dikes/veins of garnet pyroxenite
36 lithologies. Recycling of these dikes/veins with isotopically heavier Fe can readily
37 contribute to the Fe isotope heterogeneity in the MORB mantle. However, the

38 extremely high primitive $\delta^{56}\text{Fe}$ values of the two alkali basalts (up to 0.34‰) require
39 an enriched source component with unusually high $\delta^{56}\text{Fe}$ values. We suggest that
40 partial melts from the recycled dikes/veins of garnet pyroxenite lithologies can react
41 with the ambient peridotitic mantle and generate a secondary garnet pyroxenite with
42 heavier Fe isotope compositions than, but similar radiogenic isotope compositions as
43 its precursor. Melting-induced mixing between these garnet pyroxenites (recycled and
44 newly formed) and depleted mantle matrix can readily explain the compositional
45 variations in elements, radiogenic isotopes and Fe isotopes observed in these
46 seamount lavas. These new data and correlated variations offer a new dimension for
47 understanding the origin of mantle chemical and isotopic heterogeneity in the context
48 of chemical differentiation of the Earth.

49

50 **Key words:** East Pacific Rise; mid-ocean ridge basalts; Fe isotope; mantle
51 heterogeneity; seamounts; mantle metasomatism

52

53 **1. Introduction**

54 The Earth's upper mantle has been inferred to be broadly heterogeneous at
55 different length scales with respect to its incompatible element abundances and
56 radiogenic isotope compositions through studies of mid-ocean ridge basalts (MORB)
57 (Allègre and Turcotte, 1986; Donnelly et al., 2004; Mahoney et al., 1994; Niu and
58 Barzai, 1997; Niu et al., 2002a; Waters et al., 2011; Zindler et al., 1984). The origin of

59 these chemical and isotopic heterogeneities has long been attributed to the process of
60 subduction, which can reinject enriched materials such as terrigenous or pelagic
61 sediments (e.g., [Cohen and O'Nions, 1982](#); [Weaver et al., 1986](#); [Wright and White,](#)
62 [1987](#)), metasomatized oceanic lithospheric mantle (e.g., [Galer and O'Nions, 1986](#);
63 [Niu et al., 1999, 2002a](#)) or oceanic crust materials (e.g., [Allègre and Turcotte, 1986](#);
64 [Donnelly et al., 2004](#); [Hirschmann & Stolper, 1996](#); [Stracke and Bourdon, 2009](#)) to
65 the depleted asthenospheric mantle. However, whether the subduction process can
66 introduce heterogeneity of non-radiogenic isotopes in the MORB mantle remains
67 poorly constrained (e.g., [Elliott et al., 2006](#)).

68 Iron is by mass the most abundant metal of the Earth, and studies have observed
69 varied Fe isotope compositions in mantle and mantle-derived rocks (e.g., [Williams et](#)
70 [al., 2004](#); [Weyer and Ionov, 2007](#); [Teng et al., 2008](#); [Dauphas et al., 2009](#); [Sossi et al.,](#)
71 [2012, 2016](#); [Williams and Bizimis, 2014](#); [Konter et al., 2016](#); [Nebel et al., 2018,](#)
72 [2019](#)), which may provide new insights into the origin of chemical and isotopic
73 differentiation of the Earth. As the most abundant terrestrial magmas, the mid-ocean
74 ridge basalts (MORB) have been studied to show globally homogeneous Fe isotopic
75 compositions ($\delta^{56}\text{Fe} = +0.11 \pm 0.04\%$, 2SD; [Teng et al., 2013](#)). This has been
76 interpreted as reflecting a homogeneous asthenospheric mantle source ([Beard and](#)
77 [Johnson, 2007](#); [Chaddock et al., 2013](#); [Poitrasson et al., 2013](#); [Teng et al., 2013](#))
78 although mantle melting ([Dauphas et al., 2009, 2014](#); [Weyer and Ionov, 2007](#);
79 [Williams et al., 2004, 2005](#)) and magma differentiation ([Schuessler et al., 2009](#); [Sossi](#)

80 et al., 2012, 2016; Teng et al., 2008; Chen et al., 2019) have been shown to cause
81 measurable Fe isotope fractionation. On the other hand, significant Fe isotope
82 variability observed in lithospheric mantle rocks is thought to reflect an overall
83 heterogeneous upper mantle (Huang et al., 2011; Poitrasson et al., 2013; Weyer and
84 Ionov, 2007; Williams and Bizimis, 2014), leaving the homogeneous Fe isotope
85 composition of MORB explained as resulting from homogenization during melting
86 and melt-peridotite reaction in the mantle and further homogenization in crustal
87 magma chambers (Beard and Johnson, 2004; Weyer and Ionov, 2007). Therefore, the
88 fundamental question whether the MORB mantle source has homogeneous or
89 heterogeneous Fe isotope composition remains unanswered.

90 To address this question, we studied and show here that the glass samples from
91 seamounts flanking the East Pacific Rise (EPR) have significant Fe isotope variation
92 ($\delta^{56}\text{Fe} = +0.03\text{‰}$ to $+0.36\text{‰}$) that correlates with the abundances and ratios of major
93 elements, trace elements and Sr-Nd-Pb-Hf radiogenic isotopes. The heavier Fe isotope
94 compositions (higher $\delta^{56}\text{Fe}$ values) in these EPR seamount basalts are associated with
95 the progressively more enriched mantle component. This observation is a
96 straightforward manifestation of Fe isotope heterogeneity at least in the eastern
97 Pacific mantle.

98 2. Samples and methods

99 2.1 Sample description

100 The seamounts were sampled by dredging during the 1988 R/V O2 expedition
101 aboard R/V *Thomas Washington* (Batiza et al., 1990). They were located within 1 Ma
102 isochron (< 60 km) of the EPR axis between 5° and 15°N on both Pacific and Cocos
103 Plates (Fig. 1). These samples have been previously studied for major and trace
104 elements (Niu and Batiza, 1997; Table S1) and Sr-Nd-Pb-Hf radiogenic isotopes (Niu
105 et al., 2002a; Zhang et al., 2016; Table 1). This sample suite is globally ideal to
106 examine the MORB mantle Fe isotope heterogeneity for important reasons: (1) the
107 near-ridge seamount volcanism shares the common asthenospheric source with the
108 EPR axial volcanism and is far away from any known mantle plume influence; (2)
109 possible mantle source heterogeneity can be preserved in seamount lavas because of
110 small melt volumes tapped locally beneath individual seamounts, which is obscured in
111 EPR axial lavas because of the effective homogenization processes during melt
112 focusing towards the very narrow axial zone in the mantle and also in the long-lived
113 crustal magma chambers (O'Hara, 1977; Zindler et al., 1984; Macdougall and
114 Lugmair, 1985); (3) these seamount lavas vary from extremely depleted tholeiites to
115 highly enriched alkali basalts with the extent of depletion and enrichment exceeding
116 the known range of seafloor lavas in terms of the abundances and ratios of
117 incompatible elements, showing with great fidelity the mantle source heterogeneity
118 (Niu and Batiza, 1997; Niu et al., 2002a; Zhang et al., 2016).

119 2.2 Analytical methods

120 Fe isotope compositions of 21 seamount samples with large compositional
121 variations were measured in the Laboratory of Ocean Lithosphere and Mantle
122 Dynamics, Institute of Oceanology, Chinese Academy of Sciences (IOCAS). About
123 25 mg fresh glasses were hand-picked and then washed ultrasonically in Milli-Q
124 water before digestion in HF-HNO₃-HCl on a hotplate. After repeated re-flux using
125 aqua regia to obtain full digestion, the samples were finally dissolved in 1ml 9N HCl
126 ready for chromatographic separation for Fe. Fe was purified using 1 ml
127 anion-exchange resin (Bio-Rad AG MP-1M 200-400 mesh) conditioned with 9N HCl,
128 following the procedure in [Gong et al. \(2020\)](#). Matrix elements including Cr and Ni
129 were removed by washing with 5 ml 9N HCl. The columns were then washed with 5
130 ml 6N HCl to remove Cu and possible residual Cr and Ni. Fe was eluted using 2 ml
131 1N HCl. The eluted Fe solutions were analyzed using ICP-OES to ensure purity and
132 full recovery. The total procedural blank for Fe was ~ 80 ng, which is less than 0.01%
133 of the processed samples and is thus considered negligible. Prior to measurements, Fe
134 solutions were diluted to 1.4 ppm, and 19.6 ppm GSB Ni standard (an ultrapure single
135 elemental standard solution from the China Iron and Steel Research Institute) was
136 added as an internal mass bias monitor to each diluted sample (Ni:Fe = 1.4:1).

137 Fe isotopes were analyzed by a Nu Plasma MC-ICP-MS with wet nebulization.
138 Backgrounds were measured and subtracted using electrostatic analyzer (ESA)
139 deflection. Contributions from isobaric interferences (⁴⁰Ar¹⁴N on ⁵⁴Fe and ⁴⁰Ar¹⁶O on

140 ^{56}Fe) were eliminated by measuring in pseudo-high resolution mode with $M/\Delta M$ of >
141 8000. The mass bias fractionation during analysis was corrected using Ni doping
142 method by $^{60}\text{Ni}/^{58}\text{Ni}$ with the ^{58}Fe interference on ^{58}Ni corrected based on ^{56}Fe (Oeser
143 et al., 2014; Chen et al., 2017; Chen et al., 2019). The Fe isotope data are expressed
144 using the standard notation $\delta^{56}\text{Fe}$ ($= [({}^{56}\text{Fe}/{}^{54}\text{Fe})_{\text{sample}}/({}^{56}\text{Fe}/{}^{54}\text{Fe})_{\text{IRMM-01}} - 1] \times 1000$).
145 Because the commonly used reference material IRMM-014 is no longer available, this
146 study used a new reference material GSB Fe, which has been reported relative to
147 IRMM014 ($\delta^{57}\text{Fe}_{\text{IRMM014}} = \delta^{57}\text{Fe}_{\text{GSB}} + 1.073$; $\delta^{56}\text{Fe}_{\text{IRMM014}} = \delta^{56}\text{Fe}_{\text{GSB}} + 0.729$; He et
148 al., 2015). During analysis, every two sample solutions were bracketed with 14 ppm
149 GSB Fe standard solution that was also doped with the GSB Ni solution with Ni:Fe of
150 1.4:1. Every sample solution was repeatedly analyzed for four times, with the average
151 $\delta^{57}\text{Fe}$ and $\delta^{56}\text{Fe}$ values of each sample given in Table 1. Long-term analyses of an
152 in-house Alfa Fe standard give an average $\delta^{56}\text{Fe}$ value of $0.52 \pm 0.03\text{‰}$ (2SD). The
153 $\delta^{56}\text{Fe}$ value of the USGS standard BCR-2 analyzed together with our samples was
154 $0.10 \pm 0.05\text{‰}$ (2SD, $n = 13$), consistent with the recommended literature values
155 (Craddock and Dauphas, 2011; He et al., 2015). Duplicate digestion, chemical
156 separation and analysis of two samples (R15-1 & R3-4) show good reproducibility
157 (Table 1). Detailed methods for Fe elemental purification and isotope analysis are in
158 Gong et al. (2020).

159 2.3 Correction of Fe isotopes for fractional crystallization

160 Olivine is a major liquidus phase during early differentiation of MORB melt,
161 which can subtract Fe²⁺ and light Fe isotopes from the melt (Teng et al., 2008).
162 Compilation of major elements of > 400 MORB glasses from the East Pacific Rise
163 and model results showed that olivine is the major mafic liquidus phase in these
164 magmas with Mg[#] > ~ 0.58 (Niu, 2005). The EPR seamount samples analyzed for Fe
165 isotope compositions in this study have Mg[#] of 0.57-0.72 (Table 1), consistent with
166 olivine as the major mafic liquidus phase in the melt. Therefore, in order to
167 investigate the Fe isotope composition of primitive EPR seamount lavas, we corrected
168 the Fe isotopes for the effect of fractional crystallization of olivine, following the
169 method described in Sossi et al. (2016). Olivine composition in equilibrium with each
170 EPR seamount sample is calculated, using a Fe-Mg exchange partition coefficient
171 ($K_{D_{\text{Ol-Melt}}^{\text{Fe-Mg}}}$) of 0.30, and added incrementally into the melt with the olivine
172 composition re-iterated at each increment until melt Mg[#] = 0.72, in equilibrium with
173 mantle olivine of Fo = 89.6 (Roeder and Emslie, 1970). For the correction, we use a
174 starting Fe³⁺/ΣFe = 0.15 and an isotope fractionation factor between olivine and
175 melt $\Delta^{56}\text{Fe}_{\text{Ol-melt}} = 4855 \times (\langle F \rangle_{\text{Ol}} - \langle F \rangle_{\text{melt}})/T^2$ after Dauphas et al. (2014),
176 where $\langle F \rangle$ is the average force constant of Fe-O bonds ($\langle F \rangle_{\text{Ol}} = 197$ N/m,
177 $\langle F \rangle_{\text{Fe}^{2+} \text{ in melt}} = 199$ N/m, $\langle F \rangle_{\text{Fe}^{3+} \text{ in melt}} = 351$ N/m, and $\langle F \rangle_{\text{melt}} =$
178 $\text{Fe}^{3+}/\Sigma\text{Fe} \times \langle F \rangle_{\text{Fe}^{3+} \text{ in melt}} + (1 - \text{Fe}^{3+}/\Sigma\text{Fe}) \times \langle F \rangle_{\text{Fe}^{2+} \text{ in melt}}$) and the melt
179 temperature (T) at each increment is calculated using an equation of T (°C) = 1026 ×

180 $e^{[0.01894 \times \text{MgO}(\text{wt.}\%)]}$ (Niu et al., 2002b). The $\Delta^{56}\text{Fe}_{\text{Ol-melt}}$ value thus depends on
181 temperature and melt $\text{Fe}^{3+}/\Sigma\text{Fe}$ and is incrementally adjusted with every 1% addition
182 of olivine until melt $\text{Mg}^{\#} = 0.72$. However, because the $\Delta^{56}\text{Fe}_{\text{mantle peridotite-melt}}$ value
183 calculated using the above force constants can only account for 1/3 of the isotopic
184 difference between MORBs and mantle peridotites (Dauphas et al., 2014), we
185 multiply all calculated $\Delta^{56}\text{Fe}_{\text{Ol-melt}}$ by 3, following He et al. (2019). The final
186 calculated $\Delta^{56}\text{Fe}_{\text{Ol-melt}}$ values range from -0.11% to -0.07% , which are consistent
187 with those estimated from natural samples (Williams et al., 2005; Weyer and Ionov,
188 2007; Weyer and Seitz, 2012). The calculated primitive Fe isotope compositions
189 ($\delta^{56}\text{Fe}_{\text{Prim}}$) are used to reflect mantle melting processes and/or mantle source
190 characteristics.

191 3. Results

192 The measured Fe isotope data of the seamount lavas are given in Table 1.
193 Different from the globally homogeneous MORB with $\delta^{56}\text{Fe} = +0.11 \pm 0.04\%$ (2SD;
194 Teng et al., 2013), the seamount lavas show a much larger $\delta^{56}\text{Fe}$ range from $+0.03\%$
195 to $+0.36\%$. Most of these seamount lavas have $\delta^{56}\text{Fe}$ values ranging from $+0.03\%$ to
196 $+0.19\%$, similar to published MORB data (Teng et al., 2013; Nebel et al., 2013;
197 Chen et al., 2019), except for two alkali basalts (R13-1 & R15-1) which have the
198 highest $\delta^{56}\text{Fe}$ values of 0.36% and 0.34% , respectively, exceeding the known range
199 of MORB (Fig. 2a).

200 **4. Discussion**

201 **4.1 Limited effect of seafloor alteration on the Fe isotope compositions of the**
202 **EPR seamount lavas**

203 [Rouxel et al. \(2003\)](#) revealed significant influence of seafloor alteration on the
204 Fe isotope compositions of oceanic basalts, with altered basalts showing elevated
205 $\delta^{56}\text{Fe}$ values, which was explained by the preferential leaching of Fe^{2+} and light Fe
206 isotopes during alteration. Therefore, it is necessary to discuss the influence of
207 seafloor alteration on the Fe isotope compositions of these EPR seamount basalts,
208 especially the two alkali basalts with extremely high $\delta^{56}\text{Fe}$ values (R13-1 & R15-1).
209 However, there are several evidence proving that the seafloor alteration has no
210 influence on the chemical and Fe isotopic compositions of these seamount basalts.
211 First, weathered faces were filtered out and only fresh glass chips were selected
212 during the sample preparation. Second, electron microprobe analyses gave the totals
213 of major elements > 99% for the EPR seamount basalts (Table S1; [Batiza et al., 1990](#)),
214 indicating limited seafloor alteration on these samples. Third, the $\delta^{56}\text{Fe}$ values of
215 these basalts show both positive correlations with alkali elements (e.g., K) and high
216 field strength elements (HFSE; e.g., Nb) (Fig. A1), with the two alkali basalts with
217 highest $\delta^{56}\text{Fe}$ values showing highest K and Nb contents, which further exclude the
218 possible influence of seafloor alteration on the Fe isotope compositions of these
219 basalts. This is because K and Nb are both incompatible during magmatic processes,
220 whereas K is mobile and Nb is immobile during seafloor alteration processes (e.g.,

221 [Hart et al., 1974](#)). Therefore, the positive correlations of $\delta^{56}\text{Fe}$ values with both K and
222 Nb contents contradict the influence of seafloor alteration on these samples.

223 **4.2 Iron isotope signature of primitive EPR seamount lavas**

224 Studies on basalts from Kilauea Iki lava lake, Hawaii presented evidence that Fe
225 isotopes can be fractionated during fractional crystallization with heavy Fe isotopes
226 being more enriched in the more differentiated (lower MgO) melt ([Teng et al., 2008](#)).
227 This was explained that olivine phenocrysts have lower $\delta^{56}\text{Fe}$ values than their
228 parental melts because of both equilibrium and kinetic Fe isotope fractionation, and
229 fractional crystallization of olivine results in progressively isotopically heavier Fe in
230 the residual melt ([Teng et al., 2008](#)). Similar trends of Fe isotope fractionation during
231 magma differentiation have also been observed in MORB ([Chen et al., 2019](#)) and
232 magmatic rocks in various settings ([Schuessler et al., 2009](#); [Sossi et al., 2012](#);
233 [Zambardi et al., 2014](#); [Teng et al., 2013](#); [Williams et al., 2018](#)). These studies provide
234 solid evidence for mineral (olivine and clinopyroxene) fractional crystallization to
235 produce variably heavy Fe isotope compositions in the evolved melt. Even though
236 there is no correlation between $\delta^{56}\text{Fe}$ values with indices of magma differentiation
237 (e.g., $\text{Mg}^\#$) observed in these EPR seamount basalts ([Fig. 2a](#)), indicating that
238 fractional crystallization is less significant in explaining these highly varied $\delta^{56}\text{Fe}$
239 values, correction for the effect of fractional crystallization is still necessary to
240 explore the Fe isotope composition of primitive EPR seamount lavas.

241 After correction for the effect of fractional crystallization of olivine (see section
242 2.3), the $\delta^{56}\text{Fe}_{\text{prim}}$ values of these EPR seamount lavas still show a large range from +
243 0.02‰ to + 0.34‰ (see Table 1 for corrected $\delta^{56}\text{Fe}_{\text{prim}}$). It should be noted that the
244 samples selected for Fe isotope analysis are relatively less evolved ($\text{Mg}^{\#} = 0.57\text{-}0.72$),
245 and so the difference between measured and corrected $\delta^{56}\text{Fe}$ values ($\Delta^{56}\text{Fe}$) are
246 limited within 0.03‰, which is within the analytical errors. The EPR seamount lavas
247 show $\delta^{56}\text{Fe}_{\text{prim}}$ values ranging from average N-MORB like ($\delta^{56}\text{Fe}_{\text{prim N-MORB}} = 0.09 \pm$
248 0.04‰) to higher values similar to reported enriched MORB (E-MORB; $\delta^{56}\text{Fe}_{\text{prim}}$
249 E-MORB = 0.12 ± 0.06 ‰) with the two alkali basalts showing highest $\delta^{56}\text{Fe}_{\text{prim}}$ values of
250 0.34‰ and 0.32‰, respectively (Fig. 2b).

251 4.3 Can partial melting process explain the highly varied $\delta^{56}\text{Fe}_{\text{prim}}$ values?

252 Studies have found that mantle peridotites from different localities and tectonic
253 settings display a negative correlation between $\delta^{56}\text{Fe}$ and $\text{Mg}^{\#}$, with mantle peridotites
254 that had experienced the highest extent of melt extraction (highest $\text{Mg}^{\#}$) showing the
255 lightest Fe isotope compositions (e.g., [Weyer and Ionov, 2007](#); [Williams and Bizimis,](#)
256 [2014](#)). This implies that Fe isotopes could be fractionated during partial melting, with
257 heavier Fe preferentially entering the melt, leaving an isotopically light residue. This
258 conclusion was further supported by the studies of abyssal peridotites ([Craddock et al.,](#)
259 [2013](#)), which represent the melting residue for MORB. The abyssal peridotites have
260 on average the same Fe isotope compositions as chondrites with $\delta^{56}\text{Fe}_{\text{abyssal peridotites}} =$
261 0.01‰ ([Craddock et al., 2013](#)), systematically lower than that of the average MORB

262 ($\delta^{56}\text{Fe}_{\text{MORB}} = 0.11\text{‰}$; [Teng et al., 2013](#)). The preferential residence of heavy Fe
263 isotopes in the melt indicates that the heavier Fe (e.g., ^{56}Fe) behaves more
264 incompatible than the lighter Fe (e.g., ^{54}Fe). This is because the heavier Fe (i.e., ^{56}Fe
265 vs. ^{54}Fe) is preferentially incorporated in Fe-O bonds predominated by higher valent
266 Fe (i.e., Fe^{3+} vs. Fe^{2+}) at magmatic conditions ([Dauphas et al., 2009, 2014](#); [Polyakov
267 and Mineev, 2000](#); [Polyakov et al., 2007](#); [Schuessler et al., 2007](#); [Shahar et al., 2008](#);
268 [Schoenberg et al., 2009](#)), i.e., there is a physicochemical $^{56}\text{Fe}\text{-Fe}^{3+}$ affinity, and
269 because Fe^{3+} (vs. Fe^{2+}) is more incompatible during mantle melting ([Canil et al., 1994](#);
270 [Mallmann and O'Neill, 2009](#)), the melt is thus expected to have higher $\text{Fe}^{3+}/\text{Fe}^{2+}$ and
271 high $\delta^{56}\text{Fe}$ (high $^{56}\text{Fe}/^{54}\text{Fe}$). The measurement of the force constant of iron bonds in
272 olivine and basaltic glasses under various redox conditions demonstrated significant
273 equilibrium Fe isotopic fractionation between Fe^{3+} and Fe^{2+} at mantle temperatures
274 ([Dauphas et al., 2014](#)), which allows quantitative modelling of Fe isotopic
275 fractionation during mantle melting (e.g., [Dauphas et al., 2014](#); [He et al., 2019](#)).

276 On the other hand, melts derived from different source lithologies (peridotite
277 versus garnet pyroxenite) were suggested to show different extent of Fe isotopic
278 fractionation relative to their sources ([Williams and Bizimis, 2014](#); [Sossi and O'Neil,
279 2017](#)). Partial melting modelling for peridotitic and garnet pyroxenitic mineralogies
280 with the same initial Fe isotope compositions showed that at the same degree of
281 partial melting, melts from the garnet pyroxenite have heavier Fe isotope
282 compositions than melts from the peridotite ([Williams and Bizimis, 2014](#)). This is

283 attributed to the greater contribution of clinopyroxene to the melt during partial
284 melting of the garnet pyroxenite and the large Fe isotope fractionation between
285 clinopyroxene and garnet ($\delta^{56}\text{Fe}$ values of major mantle minerals: garnet \leq olivine $<$
286 opx $<$ cpx $<$ spinel; Beard and Johnson, 2004; Williams et al., 2004, 2005, 2009; Zhao
287 et al., 2010, 2017; Johnson et al., 2020). In addition, the natural pyroxenites show
288 heavier Fe isotope compositions than the peridotites (Williams and Bizimis, 2014),
289 which can further enhance the enrichment of heavy Fe isotopes in the derived melts.
290 Therefore, mantle pyroxenite components have been popularly invoked to explain the
291 heavy Fe isotope compositions observed in the worldwide OIB and MORB influenced
292 by mantle plume materials (Williams and Bizimis, 2014; Konter et al., 2016; Sossi
293 and O'Neil, 2017; Nebel et al., 2019; Gleeson et al., 2020).

294 To investigate whether partial melting process could produce the highly varied
295 Fe isotope compositions of the EPF seamount lavas, we modelled the melt $\delta^{56}\text{Fe}$
296 variation during partial melting in the peridotite and garnet pyroxenite facies, using
297 the methods described in He et al. (2019) and Williams and Bizimis (2014),
298 respectively (Fig. 3) (Detailed modelling parameters and results are in Table S2). The
299 samples with $\delta^{56}\text{Fe}_{\text{prim}} \sim 0.20\%$ and $[\text{Sm}/\text{Yb}]_{\text{N}} < \sim 1.5$ values can be quantitatively
300 modelled by partial melting of a spinel peridotite with varied $\text{Fe}^{3+}/\text{Fe}^{2+}$ (0.02-0.05)
301 and initial $\delta^{56}\text{Fe}$ values (0.00-0.05%). However, this model is apparently inadequate
302 to explain the two alkali basalts with extreme $\delta^{56}\text{Fe}_{\text{prim}}$ values (up to 0.34%) and
303 strong garnet signature, which comprise the highest $[\text{Sm}/\text{Yb}]_{\text{N}}$ and lowest Sc contents

304 (18 and 24 ppm, respectively) among all the northern EPR samples (Niu et al., 2002a).
305 Only if unreasonably high source $\text{Fe}^{3+}/\text{Fe}^{2+}$ ratios (e.g., > 0.2) were used in the
306 modelling can such elevated melt $\delta^{56}\text{Fe}$ values be achieved. Partial melting in the
307 garnet peridotite facies may explain the garnet signature of the two alkali basalts (not
308 shown) but is still inadequate to explain their high $\delta^{56}\text{Fe}_{\text{Prim}}$ values because compared
309 with melting in the spinel peridotite facies, melting in the garnet peridotite facies can
310 produce limited increase in melt $\delta^{56}\text{Fe}$ ($\leq 0.01\text{‰}$) (Sossi and O'Neal, 2017).

311 On the other hand, partial melting in the garnet pyroxenite facies can readily
312 explain the high $[\text{Sm}/\text{Yb}]_{\text{N}}$ ratios of the two alkali basalts (Fig. 3) and also has the
313 potential to explain their high $\delta^{56}\text{Fe}_{\text{Prim}}$ values, considering that melts from garnet
314 pyroxenites have heavier Fe isotope compositions than those from peridotites
315 (Williams and Bizimis, 2014; Sossi and O'Neal, 2017). With certain initial and
316 melting modes, the $\delta^{56}\text{Fe}$ values of melts from garnet pyroxenites depend mainly on
317 the source $\delta^{56}\text{Fe}$ values, the fractionation factor between garnet and clinopyroxene
318 ($\Delta^{56}\text{Fe}_{\text{garnet-cpx}}$) and the fractionation factor between melt and clinopyroxene
319 ($\Delta^{56}\text{Fe}_{\text{melt-cpx}}$) (Williams and Bizimis, 2014; Sossi and O'Neal, 2017; He et al.,
320 2017). Following He et al. (2017), we use $\Delta^{56}\text{Fe}_{\text{garnet-cpx}}$ ($\sim -0.38 \times 10^6/\text{T}^2$)
321 measured in natural samples (Beard and Johnson, 2004; Williams et al., 2009;
322 Williams and Bizimis, 2014). At the temperature of mantle melting beneath ocean
323 ridges (~ 1300 °C; McKenzie and Bickle, 1988), $\Delta^{56}\text{Fe}_{\text{garnet-cpx}}$ is $\sim -0.15\text{‰}$.
324 $\Delta^{56}\text{Fe}_{\text{melt-cpx}}$ is assumed to be zero in our modelling, following Williams and

325 Bizimis (2014), which is consistent with the observation in natural samples (Weyer
326 and Seitz, 2012). The modelling results show that assuming an average MORB-like
327 source $\delta^{56}\text{Fe}$ values (0.11‰; Teng et al., 2013), partial melting in the garnet
328 pyroxenite facies is still inadequate to explain the high $\delta^{56}\text{Fe}_{\text{Prim}}$ values of the two
329 alkali basalts, which instead require source $\delta^{56}\text{Fe}_{\text{Prim}}$ values of at least $> 0.25\%$ (Fig.
330 3).

331 Based on the above modelling and discussion, we conclude that (1) partial
332 melting in the spinel peridotite facies can explain neither the high $[\text{Sm}/\text{Yb}]_{\text{N}}$ nor the
333 high $\delta^{56}\text{Fe}_{\text{Prim}}$ values of the EPR seamount basalts, and (2) partial melting in the garnet
334 pyroxenite facies can explain the high $[\text{Sm}/\text{Yb}]_{\text{N}}$ of the two alkali basalts, whereas
335 abnormally high source $\delta^{56}\text{Fe}$ values are required to explain their high $\delta^{56}\text{Fe}_{\text{Prim}}$ values.
336 Therefore, significant Fe isotope heterogeneity must exist in the mantle source of the
337 EPR seamount lavas. The positive correlation between $\delta^{56}\text{Fe}_{\text{Prim}}$ and $[\text{Sm}/\text{Yb}]_{\text{N}}$ in Fig.
338 3 can be best explained by mixing between melts from a spinel peridotitic source and
339 those from a garnet pyroxenitic source pre-enriched in heavy Fe isotopes prior to the
340 major melting event. This is in fact consistent with the conclusion of previous studies
341 that significant chemical and lithological heterogeneities exist in the northern EPR
342 mantle source (Niu and Batiza, 1997; Castillo et al., 2000; Niu et al., 1999, 2002a;
343 Zhang et al., 2016; also see below).

344 **4.4 Mantle heterogeneity beneath the northern EPR in element, radiogenic and**
345 **Fe isotope compositions**

346 Studies on the northern EPR axial lavas (e.g., [Niu et al., 1999](#)) and seamount
347 lavas on the ridge flanks ([Niu and Batiza, 1997](#); [Niu et al., 2002a](#); [Zhang et al., 2016](#))
348 have revealed a mantle source with heterogeneous element and Sr-Nd-Pb-Hf
349 radiogenic isotope compositions. Compared with the axial lavas, the seamount lavas
350 preserve more information of the source compositional heterogeneity, showing larger
351 variations in Sr-Nd-Pb-Hf radiogenic isotopes ([Fig. 4](#)). This is because the axial lavas
352 experienced significant extent of melt mixing and homogenization within the mantle
353 during melt aggregation towards the ridges and in the crustal magma chambers before
354 their eruptions ([O'Hara, 1977, 1985](#); [Maccougall and Lugmair, 1985](#); [Sinton and](#)
355 [Detrick, 1992](#); [Batiza et al., 1996](#); [Niu, 1997](#)). In contrast, the seamount lavas
356 represent much smaller volumes of melts tapped locally by volcanos lacking
357 steady-state magma chambers and thus avoid efficient mixing ([Batiza and Vanko,](#)
358 [1984](#); [Zindler et al., 1984](#); [Niu et al., 2002a](#)).

359 The EPR seamount lavas define significant correlations among Sr-Nd-Pb-Hf
360 isotopes ([Fig. 4](#)). Two samples with highest Pb isotope ratios which were described as
361 HIMU-like in [Niu et al. \(2002a\)](#) and two alkali basalts show most enriched radiogenic
362 isotope compositions. These correlations can in first order be explained as reflecting
363 melting-induced mixing of a two-component mantle with the enriched component
364 dispersed as physically distinct domains in the depleted mantle matrix having

365 radiogenic isotope compositions similar to the ultra-depleted Garrett transform lavas
366 (Fig. 4) (Niu et al., 2002a). The coupled correlations of radiogenic isotopes with
367 incompatible elements (e.g., Ba, Nb, Rb, La) and their ratios (e.g., Rb/Sr, Ba/Zr,
368 [La/Sm]_N, [Sm/Yb]_N) indicate that both the enriched and depleted mantle components
369 are ancient and have independently developed their isotopic characteristics (Fig. A2).
370 However, it should be noted neither of the two components is necessarily
371 homogeneous in chemical and isotopic compositions. For example, the HIMU-like
372 samples and two alkali basalts show similar Sr whereas distinct Pb isotope
373 compositions (Fig. 4d), and the samples with similarly enriched Sr isotope
374 compositions (⁸⁷Sr/⁸⁶Sr values of ~ 0.7029 in Fig. A2) show large variations in
375 element abundances and their ratios (e.g., Rb/Zr = 0.67-1.97, [La/Sm]_N = 1.57-3.73).

376 As we discussed above, large Fe isotope heterogeneity should exist in the mantle
377 source beneath the northern EPR, which is corroborated by the significant correlations
378 between δ⁵⁶Fe_{prim} values and Sr-Nd-Pb-Hf isotope ratios (Fig. 5). The samples with
379 enriched radiogenic isotope compositions also show higher δ⁵⁶Fe_{prim} values. This is in
380 contrast with our recent Fe isotope study on the MORB lavas at 10° 30'N, whose Fe
381 isotope variation is mainly controlled by varying extent of fractional crystallization,
382 instead of mantle heterogeneity (Chen et al., 2019). After correction for the effect of
383 fractional fractionation, these MORB lavas show a uniform δ⁵⁶Fe_{prim} value of ~ 0.04‰
384 (Chen et al., 2019). However, as we discussed above, MORB lavas experienced
385 higher extent of melt mixing and homogenization within the mantle and in the crustal

386 magma chambers. During this process, information of mantle heterogeneity in Fe
387 isotopes and radiogenic isotopes could be erased. This is consistent with the limited
388 variations in Sr-Nd-Pb isotopes of the MORB lavas at 10° 30'N (Fig. 4). It is therefore
389 not surprising that these MORB lavas with homogeneous radiogenic isotope
390 compositions show uniform $\delta^{56}\text{Fe}_{\text{prim}}$ values.

391 It should be noted that similar to the abundances of incompatible elements and
392 their ratios, the $\delta^{56}\text{Fe}_{\text{prim}}$ values also show large variation (+0.10‰ to +0.34‰) in the
393 samples with similar $^{87}\text{Sr}/^{86}\text{Sr}$ value of ~ 0.7029 (Fig. 5). This reflects heterogeneous
394 Fe isotope compositions in the enriched mantle component and more importantly
395 implies a common process that results in the fractionation of Fe isotopes and variation
396 of incompatible element abundances in the enriched mantle component.

397 Indeed, the large $\delta^{56}\text{Fe}_{\text{prim}}$ variation of the EPR seamount lavas correlates
398 significantly with the major and trace element abundances (Fig. 6). The subscript 72
399 in Fig. 6 refers to the corresponding oxides (i.e., Na_2O , TiO_2 , Al_2O_3 and FeO)
400 corrected for the effects of crustal level differentiation to constant $\text{Mg}^\#$
401 ($\text{Mg}/[\text{Mg}+\text{Fe}^{2+}]\times 100 = 72$), following the method in Niu et al. (1999) and Niu and
402 O'Hara (2008). The corrected major element compositions thus reflect the effects of
403 mantle sources and processes because basaltic melts with $\text{Mg}^\# \geq 72$ are in equilibrium
404 with mantle olivine (the corrected major element data are in Table S3). Because their
405 significant correlations with Sr-Nd-Pb-Hf radiogenic isotopes (Fig. A3), the corrected
406 major element compositions reflect, to a great extent, the compositional variation of

407 fertile mantle sources (Niu et al., 2002a). Apparently, heavier Fe isotope composition
408 (higher $\delta^{56}\text{Fe}_{\text{prim}}$) is associated with melts derived from an enriched mantle
409 endmember with high Na_2O , TiO_2 , Al_2O_3 (also high P_2O_5 ; Fig. A4), low FeO (also
410 low MgO , CaO and $\text{CaO}/\text{Al}_2\text{O}_3$; Fig. A4), and high incompatible element abundances.
411 It follows that the origin of the Fe isotope heterogeneity in the source of these lavas
412 must have been caused by the same processes that have led to the mantle major and
413 trace element heterogeneities at least in the northern EPK mantle.

414 **4.5 Origin of the enriched mantle component with heavy Fe isotope composition**

415 **4.5.1 A low-degree melting origin of the enriched mantle component**

416 As shown in Fig. 7, $\delta^{56}\text{Fe}_{\text{prim}}$, together with Sr-Nd-Pb-Hf radiogenic isotopes,
417 correlates increasingly better with the abundances of the progressively more
418 incompatible elements. This indicates that the enriched component must have a
419 magmatic origin. Elemental ratios such as Zr/Hf, Nb/Ta, Rb/Cs and Ce/Pb are often
420 considered as constant in most magmatic processes because of the closely similar
421 incompatibility between the element in the numerator and the element in the
422 denominator (Hofmann and White, 1983; Hofmann et al., 1986; Newsom et al., 1986),
423 but it is the seamount data that demonstrate for the first time that the element in the
424 numerator is actually more incompatible than the element in the denominator (Niu
425 and Batiza, 1997). The samples having progressively sub-chondritic Zr/Hf ($< \sim 36.3$)
426 and Nb/Ta ($< \sim 17.6$), and Rb/Cs ($< \sim 80$) and Ce/Pb ($< \sim 25$) lower than mean
427 oceanic basalt (Sun and McDonough, 1989) reflect their mantle source with prior melt

428 extraction/depletion. The samples having higher of these ratios reflect their source
429 with prior low-degree (low-F) melt enrichment/metasomatism. This is a
430 straightforward concept because the effects of elemental fractionation between
431 elements with subtle incompatibility difference can be readily seen in the melting
432 residues, but not detectable in the melt unless the extent of melting is rather small (i.e.,
433 the low-F effect) (Niu et al., 2002a). Hence, the positive correlations of $\delta^{56}\text{Fe}_{\text{prim}}$
434 values (also Sr-Nd-Pb-Hf isotopes; Fig. A5) with element 1 ratios of Zr/Hf, Nb/Ta,
435 Rb/Cs and Ce/Pb (Fig. 8) reflect that the enriched component with heavy Fe isotope
436 composition must be of a low-F melt origin. Indeed, the major element characteristics
437 of this low-F melt (high Na_2O , TiO_2 , Al_2O_3 and low CaO , FeO , MgO and thus
438 $\text{CaO}/\text{Al}_2\text{O}_3$), as inferred from the data trends in Fig. 3 and Fig. A4, are in agreement
439 with experimental results (Baker et al., 1975) and glass inclusions in mantle xenoliths
440 (Schiano et al., 1998; Schiano and Bourdon, 1999).

441 As mentioned above, because Fe^{3+} (vs. Fe^{2+}) is more incompatible during mantle
442 melting (Canil et al., 1994; Mallmann and O'Neill, 2009) and because heavy Fe
443 isotopes (e.g., ^{56}Fe) favor Fe^{3+} complexes (Polyakov and Mineev, 2000; Polyakov et
444 al., 2007), the heavier Fe isotopes (e.g., ^{56}Fe) behave more incompatible than the
445 lighter Fe isotopes (e.g., ^{54}Fe). Therefore, melt is expected to have heavier Fe isotope
446 compositions than the source mantle with melt from lower degree of partial melting
447 having higher ^{56}Fe . We thus suggest that the mantle source region of the EPR
448 seamount lavas must have been pre-enriched/metasomatized by such a low-F melt

449 component with enriched incompatible element and heavy Fe isotope compositions
450 prior to the major melting event. The enriched (easily melted) low-F melt component
451 with heavy Fe isotope compositions were most likely dispersed as physically distinct
452 domains in the more depleted (refractory) matrix prior to major melting events (Fig.
453 9a). Varying extent of melting of such a two-component mantle (Fig. 9a) will produce
454 mixing relations in geochemical diagrams as illustrated in Figs. 3-6.

455 The chemically and physically most likely localities for the low-F melt
456 metasomatism lie within the seismic low velocity zone (LVZ) beneath ocean basins
457 where incipient melt forms with the low-F melt geochemical characteristics enriched
458 in volatiles (e.g., H₂O and CO₂) and incompatible elements (Fig. 9b) (Niu and O'Hara,
459 2009; Green et al., 2010). Because of ridge-suction induced asthenospheric flow
460 towards ridges (Niu and Hékinina, 2004), these low-F melts can be extracted and
461 directly contribute to the magmatism beneath oceanic ridges (Fig. 9b). In this case, the
462 low-F melts would be young features with enriched incompatible elements but
463 depleted Sr-Nd-Pb-Hf isotopes (Balliday et al., 1995). However, as the low-F melt
464 components in the mantle source of these EPR seamount lavas are ancient (Niu et al.,
465 2002a; see above), there must be a process which kept these low-F melt components
466 chemically isolated to develop long-time integrated radiogenic Sr and Pb isotopes and
467 unradiogenic Nd and Hf isotopes.

468 One reasonable explanation is that after their generation within the LVZ, these
469 low-F melts can concentrate towards the lithosphere-asthenosphere boundary (LAB)

470 and forms a melt-rich layer beneath the LAB (Fig. 9b). Such a melt-rich layer beneath
471 ocean basins has been seismically detected (Kawakatsu et al., 2009), which can
472 metasomatize the overlying growing/thickening lithosphere by crystallizing dikes and
473 veins of garnet pyroxenite lithologies embedded in the mature lithosphere (Fig. 9b)
474 (Niu, 2008; Niu and O'Hara, 2003; Niu and Green, 2018). The high Fe^{3+} and $\delta^{56}Fe$
475 signature of the low-F melts will inevitably be preserved in these dikes and veins.
476 Indeed, studies have revealed high $Fe^{3+}/\Sigma Fe$ (up to 0.40) in clinopyroxene megacrysts
477 that were crystallized from basaltic melts under high pressures (McGuire et al., 1989;
478 Dyar et al., 1996; Yang and McCammon, 2012). Recent studies on garnet pyroxenites
479 from Oahu, Hawaii with a high-pressure cumulate origin showed high $\delta^{56}Fe$ values
480 (0.05‰-0.16‰) of these mantle lithologies (Williams and Bizimis, 2014). Such a
481 metasomatized oceanic lithosphere will finally be subducted into the mantle at
482 subduction zones and reside there for a long geologic history before being recycled
483 into the mantle source region and contributing to the incompatible element,
484 Sr-Nd-Pb-Hf isotopes and heavy Fe isotope enriched components in oceanic basalts
485 such as ocean island basalts and seamount lavas in this study (Niu and O'Hara, 2003;
486 Niu et al., 2002a, 2012; Williams and Bizimis, 2014).

487 **4.5.2 Recycled oceanic crust material or carbonated peridotites are not suitable** 488 **to be the enriched source components of the EPR seamount lavas**

489 Recycled oceanic crust material has long been invoked to be the enriched source
490 endmember of E-MORB (e.g., Allègre and Turcotte, 1986; Donnelly et al., 2004;

491 [Hirschmann & Stolper, 1996](#); [Stracke and Bourdon, 2009](#)). Recently, studies on the
492 OIB lavas also use recycled oceanic crust materials as possible enriched source
493 endmember with heavy Fe isotope compositions ([Konter et al., 2016](#); [Nebel et al.,](#)
494 [2019](#)). As a represent of partial melt from the depleted sub-ridge mantle, oceanic crust
495 is expected to have heavier Fe isotope compositions than the source mantle (see
496 above). However, in the case of the EPR seamount lavas in this study, the oceanic
497 crust material is not suitable to be the enriched source component because: (1) the
498 oceanic crust endures significant dehydration during subduction with the residual
499 crust highly depleted in water-soluble incompatible elements (e.g., Ba, Rb, Cs, K, Sr,
500 Pb etc.) ([Niu et al., 2002a](#); [Niu and O'Hara, 2003](#); [Workman et al., 2004](#)). If the
501 recycled oceanic crust was geochemically responsible for those enriched EPR
502 seamount lavas, the latter should be highly depleted in these elements, which is not
503 observed ([Figs. 6 & 7](#)); (2) the oceanic crust is on average product from high degree (>
504 10%; [Niu, 1997](#)) of mantle melting with essentially constant Zr/Hf (~ 36.3), Nb/Ta (~
505 17.6), Rb/Cs (~ 80) and Ce/Pb (~ 25) ratios ([Hofmann and White, 1983](#); [Hofmann et](#)
506 [al., 1986](#); [Newsom et al., 1980](#); [Sun and McDonough, 1989](#)). However, the enriched
507 endmember of these EPR seamount lavas has higher values of these element ratios
508 ([Fig. 8](#)), indicating an apparent low-F (vs. high-F) origin (see above). Therefore,
509 although recycled oceanic crust in the mantle source region could explain the heavy
510 Fe isotope composition of mantle-derived melts, it cannot explain the incompatible
511 element characteristics of the EPR seamount lavas.

512 The Cenozoic basalts in eastern China were reported to show variably heavy Fe
513 isotope compositions with $\delta^{56}\text{Fe}$ values of 0.10‰-0.29‰, which were explained as
514 melts from an extremely oxidized peridotitic source (He et al., 2019). Together with
515 evidence from Mg and Zn isotopes, such an oxidized peridotitic source was argued to
516 be formed by the metasomatism of recycled carbonates whose reduction to diamonds
517 in the deep mantle caused the oxidization of surrounding mantle (He et al., 2019).
518 Partial melting experiments and studies on natural samples revealed that melts from a
519 carbonated mantle source show depletion in HFSEs (e.g., Ti, Zr, Hf) (e.g., Yaxley et
520 al., 1991; Baker and Wyllie, 1992; Hauri et al., 1993; Dasgupta et al., 2009). Indeed,
521 we have observed more prominent negative Ti anomalies ($\text{Ti}/\text{Ti}^* < 1$; $\text{Ti}/\text{Ti}^* = 2 \times$
522 $\text{Ti}_{\text{PM}}/[\text{Sm}_{\text{PM}} + \text{Eu}_{\text{PM}}]$) in the EPR seamount samples with heavier Fe isotope
523 compositions (Fig. A6), which is consistent with their derivation from a carbonated
524 mantle source. However, the seamount samples with heavier Fe isotope compositions
525 show more prominent positive Zr anomalies ($\text{Zr}/\text{Zr}^* > 1$; $\text{Zr}/\text{Zr}^* = 2 \times \text{Zr}_{\text{PM}}/[\text{Nd}_{\text{PM}} +$
526 $\text{Sm}_{\text{PM}}]$), which is in contrast with their derivation from a carbonated mantle source
527 (Fig. A6). In fact, modelling of Ti/Ti^* and Zr/Zr^* variations during partial melting
528 under spinel peridotite facies shows that the low-degree melts are characterized by
529 negative Ti but positive Zr anomalies (Fig. A7), consistent with the modelling results
530 in Johnson (1993). Therefore, the negative Ti but positive Zr anomalies observed in
531 the EPR seamount lavas with heavy Fe isotope compositions are consistent with their

532 derivation from an enriched source component having a low-F melt origin, instead of
533 a carbonate metasomatic origin.

534 **4.5.3 A three-stage model to generate the EPR seamount lavas with elevated** 535 **$\delta^{56}\text{Fe}_{\text{prim}}$ values**

536 The major and trace element characteristics of the EPR seamount lavas with
537 heavy Fe isotope compositions all indicate an enriched mantle source component
538 generated by low-F melting, which most likely happened in the LVZ beneath the
539 oceanic lithosphere. Modelling of the Fe isotopic fractionation during melting of a
540 normal peridotitic source with initial $\delta^{56}\text{Fe}$ of 0.02‰ (Weyer and Ionov, 2007) and
541 $\text{Fe}^{3+}/\text{Fe}^{2+}$ of 0.037 (Canil et al., 1994) showed that the low-F (e.g., 1%) melt has $\delta^{56}\text{Fe}$
542 of $\sim 0.15\text{‰}$ (Fig. 3). Such a $\delta^{56}\text{Fe}$ value of the enriched source component, although
543 can explain the Fe isotope compositions of most seamount samples, still cannot
544 satisfy the high source $\delta^{56}\text{Fe}$ value (at least $\sim 0.25\text{‰}$; Fig. 3) required by the two
545 alkali basalts (Fig. 10). Considering the two alkali basalts have $\delta^{56}\text{Fe}_{\text{prim}}$ values higher
546 than, whereas $^{87}\text{Sr}/^{86}\text{Sr}$ values similar to the other samples with $^{87}\text{Sr}/^{86}\text{Sr}$ values of \sim
547 0.7029 (Fig. 10), a recent secondary enrichment process in the source region prior to
548 the major melting event is required. Such a process is expected to cause further
549 enrichment of heavy Fe isotopes and incompatible elements with little change of the
550 radiogenic isotope compositions in the enriched source component, which is also
551 required to explain the large variations of element abundances and their ratios in the
552 samples with similar $^{87}\text{Sr}/^{86}\text{Sr}$ values of ~ 0.7029 (Fig. A3).

553 To explain the Fe isotope compositions of the Pitcairn OIB lavas, [Nebel et al.](#)
554 (2019) provided a two-stage model in which low-F melts from the recycled crustal
555 eclogite react with the ambient peridotitic mantle to form EM1-pyroxenite with
556 heavier Fe isotope compositions in stage 1 and low-F melting of this pyroxenite
557 component generates the OIB lavas with high $\delta^{56}\text{Fe}$ values in stage 2. In this study,
558 the recycled low-F melt component in the garnet pyroxenite lithologies can partially
559 melt and react with the ambient mantle to produce a secondary garnet pyroxenite with
560 higher $\delta^{56}\text{Fe}$ value ($\sim 0.25\%$; [Fig. 10](#)) and higher incompatible element abundances
561 than, but similar radiogenic isotope compositions as its precursor ([Yaxley and Green,](#)
562 [1998](#); [Herzberg, 2006](#); [Sobolev et al., 2007](#)). During the major melting event, because
563 the pyroxenite components (secondary and its precursor) have lower solidus
564 temperature (T_{solidus}), they will melt preferentially and generate enriched lavas
565 represented by the two alkali basalts and other samples with high $^{87}\text{Sr}/^{86}\text{Sr}$ values ([Fig.](#)
566 [10](#)). Increasing extent of melting of this two-component mantle (garnet pyroxenite
567 and depleted mantle matrix) cause the variations of elements, Fe isotope and
568 Sr-Nd-Pb-Hf isotope compositions observed in the EPR seamount lavas ([Fig. 9a](#)).

569 We therefore suggest a three-stage model ([Fig. 10](#)) to explain the varied $\delta^{56}\text{Fe}_{\text{prim}}$
570 values of the LPK seamount lavas: Stage 1, the low-F melts with enriched
571 incompatible elements and heavy Fe isotope compositions ($\delta^{56}\text{Fe} \sim 0.15\%$) were
572 formed in the LVZ and metasomatized the overlying oceanic lithosphere by
573 crystallizing dikes and veins of garnet pyroxenite lithologies. Such a metasomatized

574 oceanic lithosphere was finally subducted into the mantle at subduction zones and
575 resided there for a long geologic history before being recycled into the mantle source
576 region of the EPR seamount lavas; Stage 2, partial (low-F) melts from the recycled
577 ancient (~ 0.5 Ga) garnet pyroxenite component reacted with the ambient mantle to
578 form a secondary garnet pyroxenite with higher $\delta^{56}\text{Fe}$ values (~ 0.5‰) than its
579 precursor; Stage 3, melting induced mixing of the secondary garnet pyroxenite and its
580 precursor with depleted mantle matrix generated the EPR seamount lavas with varied
581 $\delta^{56}\text{Fe}_{\text{prim}}$ values (0.02‰-0.34‰).

582 We conclude that Fe isotope heterogeneity exists in a two-component EPR
583 mantle, with enriched garnet pyroxenites having variably heavy Fe isotope
584 compositions dispersed in the depleted mantle matrix (Fig. 9). Because Fe is one of
585 the major elements in seafloor basalts and in Earth's mantle, the discovery of the
586 correlated variation of Fe isotopes with other major elements, trace elements and
587 Sr-Nd-Pb-Hf radiogenic isotopes in the EPR seamount lavas is informative towards
588 resolving the fundamental question on whether global MORB major element
589 systematics reflects mantle melting conditions (Gale and Langmuir, 2014) or mantle
590 source compositional variation (Niu and O'Hara, 2008; Niu, 2016) or both.
591 Furthermore, Fe is by mass the most abundant metal of the Earth and the new data
592 and understanding presented here provide new insights into the origin of mantle
593 chemical and isotopic heterogeneity in the grand context of chemical differentiation
594 of the Earth.

595 5. Conclusions

596 We report non-radiogenic Fe isotope analyses from < 1 m.y. seamount lavas
597 taken from the flanks of the northern East Pacific Rise between 5° and 15°N. These
598 samples show large Fe isotope variation with $\delta^{56}\text{Fe}$ values (+ 0.03‰ to + 0.36‰)
599 exceeding the known range of MORB (Teng et al., 2013; Nebel et al., 2013; Chen et
600 al., 2019). Such highly varied Fe isotope compositions must reflect mantle source
601 heterogeneity and cannot be explained by seafloor alteration, magma crystallization
602 evolution or mantle partial melting processes.

603 After correction for the effect of fractional crystallization of olivine, the large
604 $\delta^{56}\text{Fe}_{\text{prim}}$ variation (+ 0.02‰ to + 0.34‰) of the EPR seamount lavas correlates
605 significantly with the abundances of major and trace elements and Sr-Nd-Pb-Hf
606 radiogenic isotopes, with heavier Fe isotope compositions (higher $\delta^{56}\text{Fe}$) being
607 associated with melts derived from a more enriched source endmember (e.g., high
608 Na_{72} , Ti_{72} , Al_{72} , $^{87}\text{Sr}/^{86}\text{Sr}$ and $^{206}\text{Pb}/^{204}\text{Pb}$, and low Ca_{72} , Fe_{72} , Mg_{72} , $^{143}\text{Nd}/^{144}\text{Nd}$,
609 $^{176}\text{Hf}/^{177}\text{Hf}$ and thus $\text{Ca}_{72}/\text{Al}_{72}$), showing significant source heterogeneity. $\delta^{56}\text{Fe}_{\text{prim}}$,
610 together with Sr-Nd-Pb-Hf radiogenic isotopes, correlates increasingly better with the
611 abundances of the progressively more incompatible elements, indicating a magmatic
612 origin of the heavy Fe isotope enriched component. In addition, higher $\delta^{56}\text{Fe}$ is
613 associated with samples with high Zr/Hf, Nb/Ta, Rb/Cs and Ce/Pb, indicating that the
614 enriched endmember must be of low-degree (low-F) melting origin, because only

615 low-F melting can effectively fractionate elements with subtle differences in
616 incompatibility in each ratio pair (Niu et al, 2002a).

617 We thus suggest that a low-F melt metasomatism at sites such as the
618 lithosphere-asthenosphere boundary beneath ocean basins can effectively cause the Fe
619 isotope fractionation. Such low-F metasomatic melt will freeze at the base of the
620 growing/thickening lithosphere as dikes and veins of garnet pyroxenite lithologies
621 embedded in the mature lithosphere, and recycling of such metasomatized mantle
622 lithosphere can readily contribute to the Fe isotope heterogeneity in the MORB
623 mantle.

624 **Acknowledgements**

625 We thank Dr. Frederic Moynier, Dr. Michael Bizimis, Dr. Hongjie Wu and four
626 anonymous reviewers for their constructive comments on previous version of this
627 manuscript. We thank Dr. Jeffrey G. Catalano and Dr. Fang Huang for editorial
628 handling. Dr. Yongsheng He is thanked for providing the GSB Fe reference material.
629 This work was supported by the NSFC-Shandong Joint Fund for Marine Science
630 Research Centers (U1606401), the National Natural Science Foundation of China
631 (NSFC Grants 41630968, 41776067), Chinese Academy of Sciences (Innovation
632 Grant Y422171011) grants from Qingdao National Laboratory for Marine Science
633 and Technology (2015ASKJ03) and 111 Project (B18048).

634 **References**

- 635 Allègre C. J. and Turcotte D. L. (1986) Implications of a two-component mantle-cake
636 mantle. *Nature* **323**, 123-127.
- 637 Baker, M.B. and Wyllie, P.J. (1992) High-pressure apatite solubility in carbonate-rich
638 liquids: Implications for mantle metasomatism. *Geochim. Cosmochim. Acta* **56**,
639 3409-3422.
- 640 Baker M., Hirschmann M., Ghiorso M. and Stolper E. (1995) Compositions of
641 near-solidus peridotite melts from experiments and thermodynamic calculations.
642 *Nature* **375**, 308-311.
- 643 Batiza R., Niu Y. and Zayac W. C. (1990) Chemistry of seamounts near the East
644 Pacific Rise: Implications for the geometry of subaxial mantle flow. *Geology* **18**,
645 1122-1125.
- 646 Batiza, R., Niu, Y., Karsten, J.L., Pogue, W., Potts, E., Norby, L. and Butler, R. (1996)
647 Steady and non-steady state magma chambers below the East Pacific Rise.
648 *Geophys. Res. Lett.* **23**, 221-224.
- 649 Beard B. L. and Johnson C. M. (2004) Inter-mineral Fe isotope variations in
650 mantle-derived rocks and implications for the Fe geochemical cycle. *Geochim.*
651 *Cosmochim. Acta* **68**, 4727-4743.
- 652 Beard B. L. and Johnson C. M. (2007) Comment on “Iron isotope fractionation during
653 planetary differentiation” by S. Weyer et al., *Earth Planet. Sci. Lett.* V240, pages
654 251–264. *Earth Planet. Sci. Lett.* **256**, 633-637.

655 Canil D., O'Neill H. S. C., Pearson D. G., Rudnick R. L., McDonough W. F. and
656 Carswell D. A. (1994) Ferric iron in peridotites and mantle oxidation states.
657 *Earth Planet. Sci. Lett.* **123**, 205-220.

658 Castillo, P., Klein, E., Bender, J., Langmuir, C., Shirey, S., Batiza, R. and White, W.
659 (2000) Petrology and Sr, Nd, and Pb isotope geochemistry of mid-ocean ridge
660 basalt glasses from the 11°45'N to 15°00'N segment of the East Pacific Rise.
661 *Geochem. Geophys. Geosyst.* **1**.

662 Chen K.-Y., Yuan H.-L., Liang P., Bao Z.-A. and Chen L. (2017) Improved
663 nickel-corrected isotopic analysis of iron using high-resolution multi-collector
664 inductively coupled plasma mass spectrometry. *Int. J. Mass. Spectrum.* **421**,
665 196-203.

666 Chen S., Niu Y., Guo P., Gong H., Sun L., Xue Q., Duan M. and Wang X. (2019) Iron
667 isotope fractionation during mid-ocean ridge basalt (MORB) evolution: Evidence
668 from lavas on the East Pacific Rise at 10°30'N and its implications. *Geochim.*
669 *Cosmochim. Acta* **267**, 227-239.

670 Cohen R. and O'Nions R. (1982) Identification of recycled continental material in the
671 mantle from Sr, Nd and Pb isotope investigations. *Earth Planet. Sci. Lett.* **61**,
672 73-84.

673 Craddock P. R. and Dauphas N. (2011) Iron Isotopic Compositions of Geological
674 Reference Materials and Chondrites. *Geostand. Geoanal. Res.* **35**, 101-123.

675 Craddock P. R., Warren J. M. and Dauphas N. (2013) Abyssal peridotites reveal the
676 near-chondritic Fe isotopic composition of the Earth. *Earth Planet. Sci. Lett.* **355**,
677 63-76.

678 Dasgupta, R., Hirschmann, M.M., McDonough, W.F., Spiegelman, M. and Withers,
679 A.C. (2009) Trace element partitioning between garnet lherzolite and carbonatite
680 at 6.6 and 8.6 GPa with applications to the geochemistry of the mantle and of
681 mantle-derived melts. *Chem. Geol.* **262**, 57-77.

682 Dauphas N., Craddock P. R., Asimow P. D., Bennett J. C., Nutman A. P. and
683 Ohnenstetter D. (2009) Iron isotopes may reveal the redox conditions of mantle
684 melting from Archean to Present. *Earth Planet. Sci. Lett.* **288**, 255-267.

685 Dauphas N., Roskosz M., Alp E. E., Neuville D. R., Hu M. Y., Sio C. K., Tissot F. L.
686 H., Zhao J., Tissandier L., Médard F. and Cordier C. (2014) Magma redox and
687 structural controls on iron isotope variations in Earth's mantle and crust. *Earth*
688 *Planet. Sci. Lett.* **398**, 127-140.

689 Dyar M. D., Martin S. V., Mackwell S. J., Carpenter S., Grant C. A. and McGuire A.
690 V. (1996) Crystal chemistry of Fe³⁺, H⁺, and D/H in mantle derived augite from
691 Dish Hill: Implications for alteration during transport, in: Dyar, M.D.,
692 McCammon, C., Schaefer, M.W. (Eds.), Mineral spectroscopy, a tribute to R.G.
693 Burns. Geochemical Society Special Publication, pp. 289–304.

694 Donnelly K. E., Goldstein S. L., Langmuir C. H. and Spiegelman M. (2004) Origin of
695 enriched ocean ridge basalts and implications for mantle dynamics. *Earth Planet.
696 Sci. Lett.* **226**, 347-366.

697 Elliott T., Thomas A., Jeffcoate A. and Niu Y. (2006) Lithium isotope evidence for
698 subduction-enriched mantle in the source of mid-ocean-ridge basalts. *Nature* **443**,
699 565-568.

700 Gale A., Langmuir C. H. and Dalton C. A. (2014) The Global Systematics of Ocean
701 Ridge Basalts and their Origin. *J. Petrol.* **55**, 1051-1062.

702 Galer S. J. G. and O'Nions R. K. (1986) Magma genesis and the mapping of chemical
703 and isotopic variations in the mantle. *Chem. Geol.* **56**, 45-61.

704 Gleeson, M.L.M., Gibson, S.A. and Williams, H.M. (2020) Novel insights from
705 Fe-isotopes into the lithological heterogeneity of Ocean Island Basalts and
706 plume-influenced MORBs. *Earth Planet. Sci. Lett.* **535**, 116114.

707 Gong, H., Guo, P., Chen, S., Duan, M., Sun, P., Wang, X. and Niu, Y. (2020) A
708 re-assessment of nickel-doping method in iron isotope analysis on rock samples
709 using multi-collector inductively coupled plasma mass spectrometry. *Acta
710 Geochim.* **39**, 353-364.

711 Green, D.H., Hibberson, W.O., Kovács, I. and Rosenthal,
712 A. (2010) Water and its influence on the lithosphere–asthenosphere boundary.
Nature **467**, 448-451.

713 Halliday A. N., Lee D.-C., Tommasini S., Davies G. R., Paslick C. R., Fitton J. G. and
714 James D. E. (1995) Incompatible trace elements in OIB and MORB and source
715 enrichment in the sub-oceanic mantle. *Earth Planet. Sci. Lett.* **133**, 379-394.

716 Hart, S.R., Erlank, A.J. and Kable, E.J.D. (1974) Sea floor basalt alteration: Some
717 chemical and Sr isotopic effects. *Contrib. Mineral. Petrol.* **41**, 219-230.

718 Hauri, E.H., Shimizu, N., Dieu, J.J. and Hart, S.R. (1993) Evidence for
719 hotspot-related carbonatite metasomatism in the oceanic upper mantle. *Nature*
720 **365**, 221-227.

721 He Y., Ke S., Teng F.Z., Wang T., Wu H., Lu Z. and Li S. (2015) High- Precision
722 Iron Isotope Analysis of Geological Reference Materials by High- Resolution
723 MC- ICP- MS. *Geostand. Geoanal. Pers.* **39**, 341-356.

724 He, Y., Wu, H., Ke, S., Liu, S.-A. and Wang, Q. (2017) Iron isotopic compositions of
725 adakitic and non-adakitic granitic magmas: Magma compositional control and
726 subtle residual garnet effect. *Geochim. Cosmochim. Acta* **203**, 89-102.

727 He, Y., Meng, X., Ke, S., Wu, H., Zhu, C., Teng, F.-Z., Hoefs, J., Huang, J., Yang, W.,
728 Xu, L., Hou, Z., Ren, Z.-Y. and Li, S. (2019) A nephelinitic component with
729 unusual $\delta^{56}\text{Fe}$ in Cenozoic basalts from eastern China and its implications for
730 deep oxygen cycle. *Earth Planet. Sci. Lett.* **512**, 175-183.

731 Hirschmann M. M. and Stolper E. M. (1996) A possible role for garnet pyroxenite in
732 the origin of the “garnet signature” in MORB. *Contrib. Mineral. Petrol.* **124**,
733 185-205.

734 Huang F., Zhang Z., Lundstrom C. C. and Zhi X. (2011) Iron and magnesium isotopic
735 compositions of peridotite xenoliths from Eastern China. *Geochim. Cosmochim.*
736 *Acta* **75**, 3318-3334.

737 Hofmann A. W. and White W. M. (1983) Ba, Rb and Cs in the Earth's Mantle, *Z.*
738 *Naturforsch. Sect. A-J. Phys. Sci.* **38**, 256.

739 Hofmann A. W., Jochum K., Seufert M. and White W. (1986) Nb and Pb in oceanic
740 basalts: new constraints on mantle evolution. *Earth Planet. Sci. Lett.* **79**, 33-45.

741 Johnson, C., Beard, B. and Weyer, S. (2020) High Temperature Fe Isotope
742 Geochemistry, in: Johnson, C., Beard, B., Weyer, S. (Eds.), *Iron Geochemistry:*
743 *An Isotopic Perspective*. Springer International Publishing, Cham, pp. 85-147.

744 Johnson, K.T. (1998) Experimental determination of partition coefficients for rare
745 earth and high-field-strength elements between clinopyroxene, garnet, and
746 basaltic melt at high pressures. *Contrib. Mineral. Petrol.* **133**, 60-68.

747 Kawakatsu H., Kumar P., Takei Y., Shinohara M., Kanazawa T., Araki E. and
748 Suyehiro K. (2009) Seismic Evidence for Sharp Lithosphere-Asthenosphere
749 Boundaries of Oceanic Plates. *Science* **324**, 499.

750 Konter J. G., Pietruszka A. J., Hanan B. B., Finlayson V. A., Craddock P. R., Jackson
751 M. G. and Dauphas N. (2016) Unusual $\delta^{56}\text{Fe}$ values in Samoan rejuvenated lavas
752 generated in the mantle. *Earth Planet. Sci. Lett.* **450**, 221-232.

753 Macdougall, J.D. and Lugmair, G.W. (1985) Extreme isotopic homogeneity among
754 basalts from the southern East Pacific Rise: mantle or mixing effect? *Nature* **313**,
755 209-211.

756 Mahoney J. J., Sinton J. M., Kurz M. D., Macdougall J. D., Spenser K. J. and
757 Lugmair G. W. (1994) Isotope and trace element characteristics of a super-fast
758 spreading ridge: East Pacific rise, 13–23°S. *Earth Planet. Sci. Lett.* **121**,
759 173-193.

760 Mallmann G. and O'Neill, H. S. C. (2009) The Crystal/Melt Partitioning of V during
761 Mantle Melting as a Function of Oxygen Fugacity Compared with some other
762 Elements (Al, P, Ca, Sc, Ti, Cr, Fe, Ga, Y, Zr and Nb). *J. Petrol.* **50**, 1765-1794.

763 McGuire A. V., Dyar M. D. and Ward K. A. (1989) Neglected $\text{Fe}^{3+}/\text{Fe}^{2+}$ ratios—A
764 study of Fe^{3+} content of megacrysts from alkali basalts. *Geology* **17**, 687-690.

765 McKenzie, D. and Bickle, M. (1988) The volume and composition of melt generated
766 by extension of the lithosphere. *J. Petrol.* **29**, 625-679.

767 Nebel O., Arculus R. J., Sossi P. A., Jenner F. E. and Whan T. H. E. (2013) Iron
768 isotopic evidence for convective resurfacing of recycled arc-front mantle beneath
769 back-arc basins. *Geophys. Res. Lett.* **40**, 5849-5853.

770 Nebel O., Sossi P. A., Foden J., Bénard A., Brandl P. A., Stammerer J. A., Lupton J.,
771 Richter M. and Arculus R. J. (2018) Iron isotope variability in ocean floor lavas
772 and mantle sources in the Lau back-arc basin. *Geochim. Cosmochim. Acta* **241**,
773 150-163.

774 Nebel O., Sossi P. A., Bénard A., Arculus R. J., Yaxley G. M., Woodhead J. D.,
775 Rhodri Davies D. and Ruttor S. (2019) Reconciling petrological and isotopic
776 mixing mechanisms in the Pitcairn mantle plume using stable Fe isotope. *Earth
777 Planet. Sci. Lett.* **521**, 60-67.

778 Newsom H. E., White W. M., Jochum K. P. and Hofmann A. W. (1985) Siderophile
779 and chalcophile element abundances in oceanic basalt, Pb isotope evolution and
780 growth of the Earth's core. *Earth Planet. Sci. Lett.* **80**, 299-313.

781 Niu Y. (1997) Mantle melting and melt extraction processes beneath ocean ridges:
782 evidence from abyssal peridotites. *J. Petrol.* **38**, 1047-1074.

783 Niu, Y. (2005) Generation and evolution of basaltic magmas: some basic concepts
784 and a new view on the origin of Mesozoic–Cenozoic basaltic volcanism in
785 eastern China. *Geological Journal of China Universities* **11**, 9-46.

786 Niu Y. (2008) The origin of alkaline lavas. *Science* **320**, 883-884.

787 Niu Y. (2016) The Meaning of Global Ocean Ridge Basalt Major Element
788 Compositions. *J. Petrol.* **57**, 2081-2103.

789 Niu Y. and Batiza R. (1997) Trace element evidence from seamounts for recycled
790 oceanic crust in the Eastern Pacific mantle. *Earth Planet. Sci. Lett.* **148**, 471-483.

791 Niu Y. and O'Hara M. J. (2003) Origin of ocean island basalts: A new perspective
792 from petrology, geochemistry, and mineral physics considerations. *J. Geophys.
793 Res.* **108 (B4)**, 2209.

- 794 Niu Y. and Hékinian R. (2004) Ridge suction drives plume-ridge interactions. In:
795 Hékinian, R., Stoffers, P. (Eds.), *Oceanic Hotspots*. Springer-Verlag New York,
796 pp. 285-307 (Chapter 9).
- 797 Niu, Y. and O'Hara M. J. (2008) Global correlations of ocean ridge basalt chemistry
798 with axial depth: a new perspective. *J. Petrol.* **49**, 633-664.
- 799 Niu, Y. and O'Hara, M.J. (2009) MORB mantle hosts the missing Eu (Sr, Nb, Ta and
800 Ti) in the continental crust: new perspectives on crustal growth, crust–mantle
801 differentiation and chemical structure of oceanic upper mantle. *Lithos* **112**, 1-17.
- 802 Niu Y. and Green D. H. (2018) The petrological control on the
803 lithosphere-asthenosphere boundary (LAB) beneath ocean basins. *Earth Sci. Rev.*
804 **185**, 301-307.
- 805 Niu, Y., Waggoner, D.G., Sinton, J.M. and Mahoney, J.J. (1996) Mantle source
806 heterogeneity and melting processes beneath seafloor spreading centers: the East
807 Pacific Rise, 18°–19° S. *J. Geophys. Res.* **101**, 27711-27733.
- 808 Niu Y., Collerson K. D., Batiza R., Wendt J. I. and Regelous M. (1999) Origin of
809 enriched-type mid-ocean ridge basalt at ridges far from mantle plumes: The East
810 Pacific Rise at 11°20' N. *J. Geophys. Res.* **104**, 7067-7087.
- 811 Niu Y., Regelous M., Wendt I. J., Batiza R. and O'Hara M. J. (2002a) Geochemistry
812 of near-EPK seamounts: importance of source vs. process and the origin of
813 enriched mantle component. *Earth Planet. Sci. Lett.* **199**, 327-345.

814 Niu Y., Gilmore T., Mackie S., Greig A. and Bach W. (2002b) Mineral chemistry,
815 whole-rock compositions, and petrogenesis of Leg 176 gabbros: data and
816 discussion. In *Proceedings of the Ocean Drilling Program, Scientific Results 176*
817 (eds. J.H. Natland, H.J.B. Dick et al.). College Station, TX, pp. 1-60.

818 Oeser M., Weyer S., Horn I. and Schuth S. (2014) High-precision Fe and Mg isotope
819 ratios of silicate reference glasses determined in situ by femtosecond
820 LA-MC-ICP-MS and by solution nebulisation MC-ICP-MS. *Geostand. Geoanal.*
821 *Res.* **38**, 311-328.

822 O'Hara, M.J. (1977) Geochemical evolution during fractional crystallisation of a
823 periodically refilled magma chamber. *Nature* **266**, 503.

824 O'Hara, M.J. (1985) Importance of the 'shape' of the melting regime during partial
825 melting of the mantle. *Nature* **314**, 58-62.

826 Pertermann, M. and Hirschmann, M.M. (2003) Partial melting experiments on a
827 MORB-like pyroxenite between 2 and 3 GPa: Constraints on the presence of
828 pyroxenite in basalt source regions from solidus location and melting rate. *J.*
829 *Geophys. Res.* **108**, 1125.

830 Poitrasson F., Delpech G. and Grégoire M. (2013) On the iron isotope heterogeneity
831 of lithospheric mantle xenoliths: implications for mantle metasomatism, the
832 origin of basalts and the iron isotope composition of the Earth. *Contrib. Mineral.*
833 *Petro.* **165**, 1243-1258.

- 834 Polyakov V. B. and Mineev S. D. (2000) The use of Mössbauer spectroscopy in stable
835 isotope geochemistry. *Geochim. Cosmochim. Acta* **64**, 849-865.
- 836 Polyakov V. B., Clayton R. N., Horita J. and Mineev S. D. (2007) Equilibrium iron
837 isotope fractionation factors of minerals: Reevaluation from the data of nuclear
838 inelastic resonant X-ray scattering and Mössbauer spectroscopy. *Geochim.
839 Cosmochim. Acta* **71**, 3833-3846.
- 840 Regelous, M., Niu, Y., Wendt, J.I., Batiza, R., Greig, A. and Collerson, K.D. (1999)
841 Variations in the geochemistry of magmatism on the East Pacific Rise at
842 10°30'N since 800 ka. *Earth Planet. Sci. Lett.* **163**, 45-63.
- 843 Roeder P. and Emslie R. (1970) Olivine-liquid equilibrium. *Contrib. Mineral. Petrol.*
844 **29**, 275-289.
- 845 Salters, V.J. and Stracke, A. (2004) Composition of the depleted mantle. *Geochem.
846 Geophys. Geosyst.* **5**.
- 847 Stracke A. and Bourdon B. (2009) The importance of melt extraction for tracing
848 mantle heterogeneity. *Geochim. Cosmochim. Acta* **73**, 218-238.
- 849 Schoenberg R., Marks M. A. V., Schuessler J. A., von Blanckenburg F. and Markl G.
850 (2009) Fe isotope systematics of coexisting amphibole and pyroxene in the
851 alkaline igneous rock suite of the Ilímaussaq Complex, South Greenland. *Chem.
852 Geol.* **253**, 65-77.
- 853 Schuessler J. A., Schoenberg R., Behrens H. and Blanckenburg F. V. (2007) The
854 experimental calibration of the iron isotope fractionation factor between

855 pyrrhotite and peralkaline rhyolitic melt. *Geochim. Cosmochim. Acta* **71**,
856 417-433.

857 Schuessler J. A., Schoenberg R. and Sigmarsson O. (2009) Iron and lithium isotope
858 systematics of the Hekla volcano, Iceland — Evidence for Fe isotope
859 fractionation during magma differentiation. *Chem. Geol.* **256**, 78-91.

860 Shahar A., Young E.D. and Manning C. E. (2008) Equilibrium high-temperature Fe
861 isotope fractionation between fayalite and magnetite: An experimental
862 calibration. *Earth Planet. Sci. Lett.* **268**, 330-333.

863 Sinton, J.M. and Detrick, R.S. (1992) Mid-ocean ridge magma chambers. *J. Geophys.*
864 *Res.* **97**, 197-216.

865 Sossi P. A., Foden J. D. and Halverson G. P. (2012) Redox-controlled iron isotope
866 fractionation during magmatic differentiation: an example from the Red Hill
867 intrusion, S. Tasmania. *Contrib. Mineral. Petrol.* **164**, 757-772.

868 Sossi P. A., Nebel O. and Foden J. (2016) Iron isotope systematics in planetary
869 reservoirs. *Earth Planet. Sci. Lett.* **452**, 295-308.

870 Sossi, P.A. and O'Neill, H.S. (2017) The effect of bonding environment on iron
871 isotope fractionation between minerals at high temperature. *Geochim.*
872 *Cosmochim. Acta* **196**, 121-143.

873 Sun S.-S. and McDonough W. (1989) Chemical and isotopic systematics of oceanic
874 basalt: implications for mantle composition and processes. In: Saunders, A.D.,

- 875 Norry, M.J. (Eds.), *Magmatism in the Ocean Basins*. Blackwell, London, pp.
876 313–345.
- 877 Teng F.-Z., Dauphas N. and Helz R. T. (2008) Iron Isotope Fractionation During
878 Magmatic Differentiation in Kilauea Iki Lava Lake. *Science* **320**, 1620-1622.
- 879 Teng F.-Z., Dauphas N., Huang S. and Marty B. (2013) Iron isotopic systematics of
880 oceanic basalts. *Geochim. Cosmochim. Acta* **107**, 12-25.
- 881 Waters C. L., Sims K. W., Perfit M. R., Blichert-Toft J. and Blusztajn J. (2011)
882 Perspective on the genesis of E-MORB from chemical and isotopic heterogeneity
883 at 9–10° N East Pacific Rise. *J. Petrol.* **52**, 555-602.
- 884 Weaver B. L., Wood D. A., Tarney J. and Joron J. L. (1986) Role of subducted
885 sediment in the genesis of ocean-island basalts: Geochemical evidence from
886 South Atlantic Ocean islands. *Geology* **14**, 275-278.
- 887 Wendt, J.I., Regelous, M., Niu, Y., Hékinian, R. and Collerson, K.D. (1999)
888 Geochemistry of lavas from the Garrett Transform Fault: insights into mantle
889 heterogeneity beneath the eastern Pacific. *Earth Planet. Sci. Lett.* **173**, 271-284.
- 890 Weyer S. and Ionov D. A. (2007) Partial melting and melt percolation in the mantle:
891 The message from Fe isotopes. *Earth Planet. Sci. Lett.* **259**, 119-133.
- 892 Weyer, S. and Seitz, H.M. (2012) Coupled lithium- and iron isotope fractionation
893 during magmatic differentiation. *Chem. Geol.* **294-295**, 42-50.

894 Williams H. M. and Bizimis M. (2014) Iron isotope tracing of mantle heterogeneity
895 within the source regions of oceanic basalts. *Earth Planet. Sci. Lett.* **394**,
896 396-407.

897 Williams H. M., McCammon C. A., Peslier A. H., Halliday A. N., Teutsch N.,
898 Levasseur S. and Burg J.-P. (2004) Iron Isotope Fractionation and the Oxygen
899 Fugacity of the Mantle. *Science* **304**, 1656-1659.

900 Williams H. M., Peslier A. H., McCammon C., Halliday A. N., Levasseur S., Teutsch
901 N. and Burg J. P. (2005) Systematic iron isotope variations in mantle rocks and
902 minerals: The effects of partial melting and oxygen fugacity. *Earth Planet. Sci.*
903 *Lett.* **235**, 435-452.

904 Williams, H.M., Nielsen, S.G., Renac, C., Griffin, W.L., O'Reilly, S.Y., McCammon,
905 C.A., Pearson, N., Viljoen, F., Alt, J.C. and Halliday, A.N. (2009) Fractionation
906 of oxygen and iron isotopes by partial melting processes: Implications for the
907 interpretation of stable isotope signatures in mafic rocks. *Earth Planet. Sci. Lett.*
908 **283**, 156-166.

909 Williams H. M., Prytulak J., Woodhead J. D., Kelley K. A., Brounce M. and Plank T.
910 (2018) Interplay of crystal fractionation, sulfide saturation and oxygen fugacity
911 on the iron isotope composition of arc lavas: An example from the Marianas.
912 *Geochim. Cosmochim. Acta* **226**, 224-243.

913 Workman, R.K., Hart, S.R., Jackson, M., Regelous, M., Farley, K., Blusztajn, J., Kurz,
914 M., Staudigel, H., 2004. Recycled metasomatized lithosphere as the origin of the

915 Enriched Mantle II (EM2) end- member: Evidence from the Samoan Volcanic
916 Chain. *Geochem. Geophys. Geosyst.* **5**.

917 Wright E. and White W. M. (1987) The origin of Samoa: new evidence from Sr, Nd,
918 and Pb isotopes. *Earth Planet. Sci. Lett.* **81**, 151-162.

919 Yaxley, G.M., Crawford, A.J. and Green, D.H. (1991) Evidence for carbonatite
920 metasomatism in spinel peridotite xenoliths from western Victoria, Australia.
921 *Earth Planet. Sci. Lett.* **107**, 305-317.

922 Yang X. and McCammon C. (2012) Fe³⁺-rich augite and high electrical conductivity
923 in the deep lithosphere. *Geology* **40**, 131-134.

924 Zambardi T., Lundstrom C. C., Li X. and McCurry M. (2014) Fe and Si isotope
925 variations at Cedar Butte volcano; insight into magmatic differentiation. *Earth
926 Planet. Sci. Lett.* **405**, 169-179.

927 Zhang Y., Meng F. and Niu Y. (2010) Hf isotope systematics of seamounts near the
928 East Pacific Rise (EPR) and geodynamic implications. *Lithos* **262**, 107-119.

929 Zhao, X., Zhang, H., Zhu, X., Tang, S. and Tang, Y. (2010) Iron isotope variations in
930 spinel peridotite xenoliths from North China Craton: implications for mantle
931 metasomatism. *Contrib. Mineral. Petrol.* **160**, 1-14.

932 Zhao, X.M., Cao, H.H., Mi, X., Evans, N.J., Qi, Y.H., Huang, F. and Zhang, H.F.
933 (2017) Combined iron and magnesium isotope geochemistry of pyroxenite
934 xenoliths from Hannuoba, North China Craton: implications for mantle
935 metasomatism. *Contrib. Mineral. Petrol.* **172**, 40.

936 Zindler A., Staudigel H. and Batiza, R. (1984) Isotope and trace element
937 geochemistry of young Pacific seamounts: implications for the scale of upper
938 mantle heterogeneity. *Earth Planet. Sci. Lett.* **70**, 175-195.

939 **Figure captions**

940 **Figure 1** (A) Tectonic framework of the northern (5° - 15° N) EPR and the vicinity.
941 (B) Simplified map of the study area showing the locations of the near-ridge
942 seamounts. The size of the circles approximates the relative size of seamounts.
943 Seamounts with HIMU-like and alkali basalts are indicated. Modified from [Niu et al.](#)
944 (2002a).

945 **Figure 2** (a) Measured $\delta^{56}\text{Fe}$ values ($\delta^{56}\text{Fe}_{\text{meas}}$) vs. $\text{Mg}^{\#}$ of the near-EPR seamounts.
946 There is no correlation between $\delta^{56}\text{Fe}_{\text{meas}}$ and $\text{Mg}^{\#}$. (b) Primitive $\delta^{56}\text{Fe}$ values
947 ($\delta^{56}\text{Fe}_{\text{prim}}$) corrected for the effect of olivine fractionation. For comparison, the raw
948 $\delta^{56}\text{Fe}$ and $\text{Mg}^{\#}$ values of various types of MORB from literature ([Teng et al., 2013](#);
949 [Nebel et al., 2013](#); [Chen et al., 2019](#)) and those compiled in [Sossi et al. \(2016\)](#) are
950 plotted in Fig. 2a (E = enriched; T= transitional; N = normal). The corrected $\delta^{56}\text{Fe}$
951 values of various types of MORB are plotted for comparison in Fig. 2b. Because the
952 MORB samples in [Chen et al. \(2019\)](#) were highly evolved with $\text{Mg}^{\#}$ of 0.22-0.61, we
953 did not correct the $\delta^{56}\text{Fe}$ values of these samples for the effect of fractional
954 crystallization of olivine. The error bars on each data point represent two standard
955 deviation. Green field represents the primary N-MORB average.

956 **Figure 3** Comparison of the $\delta^{56}\text{Fe}_{\text{prim}}$ and $[\text{Sm}/\text{Yb}]_{\text{N}}$ (primitive mantle normalized
957 Sm/Yb) of the EPR seamount samples with those of modelled melts from different
958 source lithologies (spinel peridotite and garnet pyroxenite). Modellings of the melt
959 $\delta^{56}\text{Fe}$ variation during partial melting in the spinel peridotite and garnet pyroxenite
960 facies follow the methods described in He et al. (2019) and Williams and Bizimis
961 (2014), respectively. For partial melting in the spinel peridotite facies, three different
962 source compositions are applied, ranging from oxidized ($\text{Fe}^{3+}/\text{Fe}^{2+} = 0.5$) with high
963 $\delta^{56}\text{Fe}$ value (0.05‰), normal with primitive mantle-like $\text{Fe}^{3+}/\text{Fe}^{2+}$ (0.037; Canil et al.,
964 1994) and $\delta^{56}\text{Fe}$ (0.02‰; Weyer and Ionov, 2007), to reduced ($\text{Fe}^{3+}/\text{Fe}^{2+} = 0.2$) with
965 low $\delta^{56}\text{Fe}$ value (0.00‰), similar as the modelling in Sossi and O'Neal (2017). ~
966 10%-15% partial melting of a normal peridotitic mantle generates melts with $\delta^{56}\text{Fe}$
967 similar to the average primary N-MORB (black diamond; $\delta^{56}\text{Fe}_{\text{prim N-MORB}} = 0.09 \pm$
968 0.04‰). For partial melting in the garnet pyroxenite facies, $\Delta^{56}\text{Fe}_{\text{garnet-cpx}}$ of -0.15%
969 and $\Delta^{56}\text{Fe}_{\text{melt-cpx}}$ of 0.00‰ are used. A garnet pyroxenite source with average
970 MORB-like $\delta^{56}\text{Fe}$ ($\sim 0.11\%$; Teng et al., 2013) cannot explain the high $\delta^{56}\text{Fe}_{\text{prim}}$
971 values of the two alkali basalts which instead require high source $\delta^{56}\text{Fe}$ value of at
972 least $\sim 0.25\%$. Modelling of melt $[\text{Sm}/\text{Yb}]_{\text{N}}$ variation by batch melting of a depleted
973 mantle (Salters and Stracke, 2004) under spinel peridotite facies uses initial source
974 modes and incongruent melting relationship from Niu (1997) and partition
975 coefficient of Sm and Yb from the compilation in Niu et al. (1996). Modelling of
976 melt $[\text{Sm}/\text{Yb}]_{\text{N}}$ variation by batch melting in the garnet pyroxenite facies uses average

977 N-MORB like source compositions (Sun and McDonough, 1989), initial source
978 modes and melting relationship from Williams and Bizimis (2014) and partition
979 coefficients of Sm and Yb from Pertermann and Hirschmann (2003). See Table S2 for
980 detailed modelling parameters and results.

981 **Figure 4** Plots of the EPR seamount lavas in the Sr-Nd-Pb-Hf isotopic spaces. For
982 comparison, EPR axial basalts at 10° 30'N (Regelous et al., 1999) and 11° 20'N (Niu
983 et al., 1999) and lavas from Garrett Transform Fault (Wendt et al., 1999) are also
984 plotted. The Sr-Nd-Pb isotope data of the EPR seamount lavas are from Niu et al.
985 (2002a). The Hf isotope data are from Zhang et al. (2017).

986 **Figure 5** Correlated variations of $\delta^{56}\text{Fe}_{\text{prim}}$ ($\delta^{56}\text{Fe}$ values corrected for the effect of
987 fractional crystallization of olivine) with Sr-Nd-Pb-Hf radiogenic isotopes of the EPR
988 seamount lavas.

989 **Figure 6** Correlated variations of $\delta^{56}\text{Fe}_{\text{prim}}$ ($\delta^{56}\text{Fe}$ values corrected for the effect of
990 fractional crystallization of olivine) with the abundances of major element oxides
991 corrected for the effects of crustal level fractionation to $\text{Mg}^{\#} = 72$ ($100 \times$
992 $\text{Mg}/[\text{Mg}+\text{Fe}^{2+}]$, i.e., the subscript 72) and incompatible trace elements.

993 **Figure 7** Correlation coefficients (R-values) of $\delta^{56}\text{Fe}_{\text{prim}}$ ($\delta^{56}\text{Fe}$ corrected for the effect
994 of fractional crystallization of olivine) and Sr-Nd-Pb-Hf isotopic ratios with
995 incompatible element abundances of the EPR seamount lavas in the order of
996 increasing relative incompatibility from right to the left. The $\delta^{56}\text{Fe}_{\text{prim}}$ values show

997 progressively better correlations with the more incompatible elements, which suggests
998 that the heavy Fe isotope enriched component is of magmatic origin. The significant
999 coupling between Sr-Nd-Pb-Hf isotopic ratios and incompatible element abundances
1000 demonstrates the ancient nature of both the depleted and enriched source materials.

1001 **Figure 8** Correlated variations of $\delta^{56}\text{Fe}_{\text{prim}}$ ($\delta^{56}\text{Fe}$ values corrected for the effect of
1002 fractional crystallization of olivine) with element ratios with elements on the
1003 numerator and denominator of each ratio pair having similar incompatibilities (Zr/Hf,
1004 Nb/Ta, Rb/Cs and Ce/Pb). The element pairs Zr/Hf, Nb/Ta, Rb/Cs and Ce/Pb do not
1005 fractionate from each other in most magmatic processes except in the case of very
1006 low-degree (low-F) melting (Niu et al., 2002a), which manifests low-F melt action in
1007 causing the observed Fe isotope fractionation.

1008 **Figure 9** (a) Schematic illustration of the concept of a two-component heterogeneous
1009 mantle source with enriched enclaves dispersed in the refractory and
1010 predominantly depleted peridotite matrix. Figure 9a[I] and 9a[II] illustrate the
1011 enriched component with different sizes and shapes. Figure 9a[III] illustrates the
1012 enriched component in the heterogeneous domains. Because the enriched dikes/veins
1013 have lower solidus temperature (T_{solidus}), they will melt preferentially during melting
1014 of such a two-component mantle. As a result, the enriched component dominates the
1015 composition of melt produced in the early stages and decreases with further melting
1016 as a result of dilution. Concurrently, the source region is progressively more depleted
1017 in the enriched dikes/veins, and further melting of this depleted source material can

1018 only produce melts progressively depleted in volatiles and incompatible elements with
1019 decreasing $\delta^{56}\text{Fe}$, $^{87}\text{Sr}/^{86}\text{Sr}$ and $^{206}\text{Pb}/^{204}\text{Pb}$ (Fig. 9a[IV]). (b) Schematic
1020 representations of our preferred model for the origin of the enriched components in the
1021 sources of oceanic basalts. The green layer (Fig. 9b) beneath the LAI indicates the
1022 presence of a melt-rich layer (supplied by the rising incipient melts denoted by the
1023 green arrowed wavy lines). These incipient melts are originated in the low velocity
1024 zone (LVZ) and have low-degree (low-F) melt characteristics with enrichment in
1025 incompatible elements and volatiles. During the oceanic lithosphere thickening with
1026 age due to heat loss to the surface, these low-F melts can be incorporated at the base
1027 of the growing lithosphere, where they crystallize and form fine dikes and veins of
1028 garnet pyroxenite lithology enriched in volatiles and incompatible elements with high
1029 $\delta^{56}\text{Fe}$. This low-F metasomatism is taking place today and likely also in Earth's
1030 history. Therefore, the deep portions of the oceanic lithosphere are important
1031 reservoirs of volatiles, heavy Fe isotopes and incompatible elements with high Rb/Sr,
1032 U/Pb, Nd/Sm and Hf/Lu responsible for their future radiogenic Sr and Pb and
1033 unradiogenic Nd and Hf isotopes. Recycling of such metasomatized mantle
1034 lithosphere into the asthenospheric mantle source regions of oceanic basalts explains
1035 the MORB mantle compositional heterogeneity. The blue-arrowed dash lines indicate
1036 ridge-suction induced asthenosphere flow towards ridges (Niu and Hékinian, 2004)
1037 with small arrows indicating sub-ridge extraction of dominantly depleted (red) and

1038 minor enriched (green) melts parental to MORBs. Modified from [Niu and Green](#)
1039 ([2018](#)).

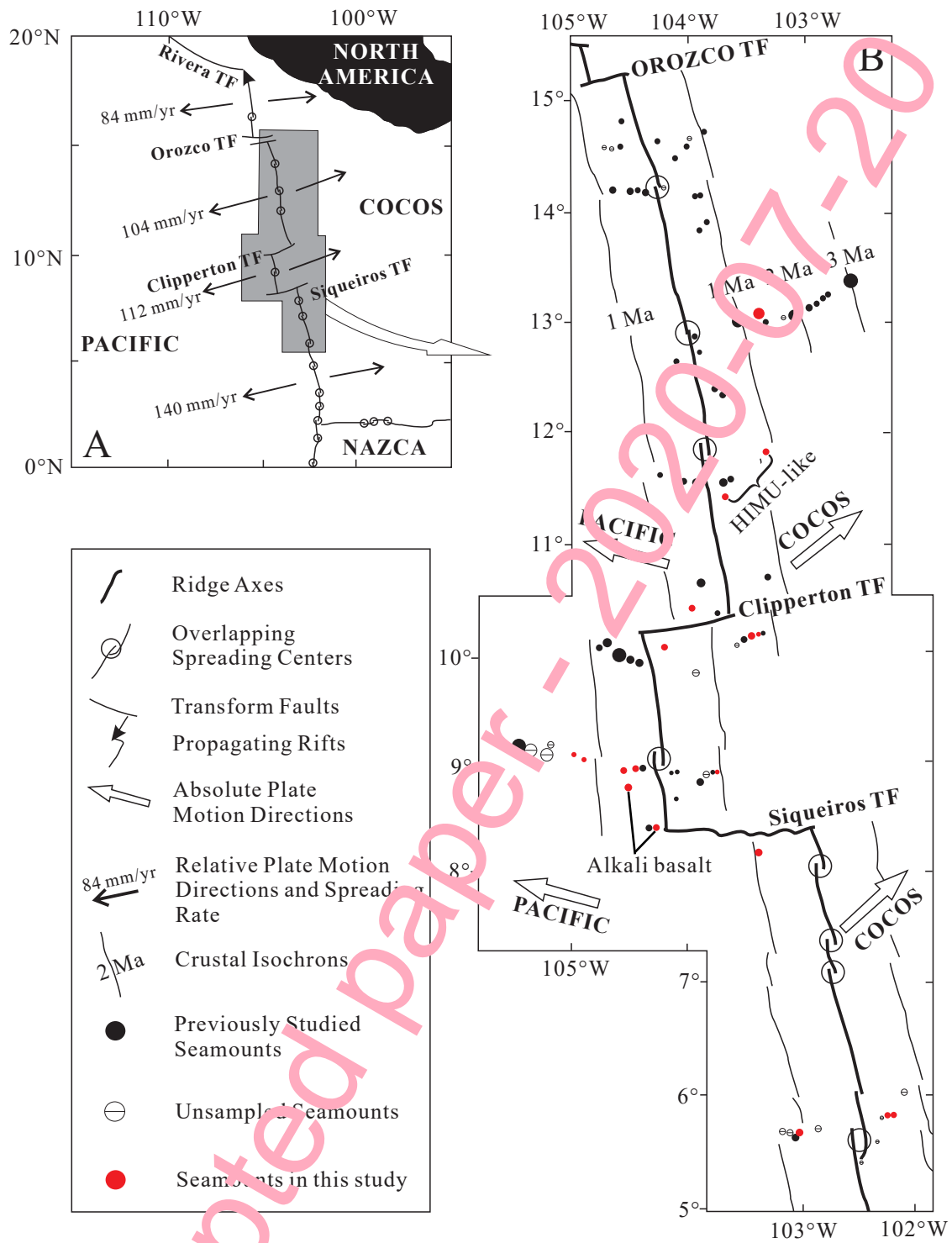
1040 **Figure 10** A three-stage model to explain the varied $\delta^{56}\text{Fe}_{\text{prim}}$ and $^{87}\text{Sr}/^{86}\text{Sr}$ of the EPR
1041 seamount lavas. Stage 1: low-F (1%) melting of a peridotitic mantle in the LVZ with
1042 present-day DMM-like Rb and Sr values ([Salters and Stracke, 2004](#)), $^{87}\text{Sr}/^{86}\text{Sr}$ of (\sim
1043 0.7020) and $\delta^{56}\text{Fe}$ of 0.02‰ ([Weyer and Ionov, 2007](#)), 0.5 Ga ago. The low-F melt
1044 that was preserved as dikes/veins of garnet pyroxenite lithologies at the bottom of
1045 oceanic lithosphere would have $\delta^{56}\text{Fe}$ of \sim 0.15‰ and present-day $^{87}\text{Sr}/^{86}\text{Sr}$ of \sim
1046 0.70303. The DMM $^{87}\text{Sr}/^{86}\text{Sr}$ value 0.5 Ga ago (\sim 0.7020) is calculated by using the
1047 present-day DMM $^{87}\text{Rb}/^{86}\text{Sr}$ ([Salters and Stracke, 2004](#)) and $^{87}\text{Sr}/^{86}\text{Sr}$ estimated from
1048 the depleted Garrett Transform lavas (\sim 0.7022; [Wendt et al., 1999](#)). Stage 2:
1049 low-degree melting of the recycled garnet pyroxenite and melt reaction with the
1050 ambient peridotite prior to the major melting event to form a secondary garnet
1051 pyroxenite with higher $\delta^{56}\text{Fe}$ of \sim 0.25‰. Stage 3: partial melting of the secondary
1052 garnet pyroxenite generated melts with high $\delta^{56}\text{Fe}$ (e.g., the two alkali basalts). See
1053 detailed modelling parameters and results in Table S4.

Table 1 Fe-Sr-Nd-Hf-Pb isotopic data of samples from near-EPR seamounts between 5 and 15°N

Sample	Type	Latitude (°N)	Longitude (°W)	Depth (m)	$\delta^{56}\text{Fe}$	2sd	$\delta^{57}\text{Fe}$	2sd	$\delta^{56}\text{Fe}_{\text{Prim}}$	$\Delta^{56}\text{Fe}$	$^{87}\text{Sr}/^{86}\text{Sr} (\pm 2\sigma)$	$^{143}\text{Nd}/^{144}\text{Nd} (\pm 2\sigma)$	$^{176}\text{Hf}/^{177}\text{Hf} (\pm 2\sigma)$	$^{206}\text{Pb}/^{204}\text{Pb}$	$^{207}\text{Pb}/^{204}\text{Pb}$	$^{208}\text{Pb}/^{204}\text{Pb}$
R1-14	N	5.77	102.18	1834	0.11	0.04	0.15	0.06	0.11	0.00	0.702393 ± 11	0.513148 ± 14	0.283187 ± 12	18.11	15.45	37.55
R13-1	Alkali	8.40	104.07	2140	0.36	0.06	0.54	0.12	0.34	0.02	0.702895 ± 07	0.512956 ± 09	0.282974 ± 07	18.58	15.55	38.01
R15-1	Alkali	8.76	104.54	1682	0.34	0.06	0.51	0.11	0.32	0.02	0.702877 ± 10	0.512979 ± 12	0.282966 ± 08	18.68	15.55	38.08
Replicate					0.33	0.03	0.46	0.09								
R62-7	E	10.03	104.19	2320	0.05	0.07	0.08	0.13	0.05	0.01	0.702420 ± 10	0.513153 ± 08	0.283167 ± 15	18.30	15.48	37.71
R18-3	E	8.93	104.46	2720	0.10	0.05	0.19	0.07	0.08	0.02	0.702722 ± 14	0.513041 ± 11	0.283061 ± 11	18.58	15.53	38.05
R25-1	N	8.88	103.79	1980	0.12	0.04	0.17	0.11	0.11	0.01	0.702432 ± 11	0.513144 ± 08	0.283158 ± 13	18.28	15.49	37.79
R3-1	N	5.78	102.21	1773	0.09	0.06	0.12	0.06	0.08	0.00	0.702458 ± 13	0.513183 ± 14	0.283194 ± 14	18.08	15.42	37.52
R31-1	E	9.09	105.02	2366	0.06	0.02	0.08	0.06	0.05	0.01	0.702362 ± 11	0.513147 ± 08	-	18.32	15.50	37.86
R32-1	E	9.09	104.92	3025	0.17	0.02	0.24	0.03	0.16	0.01	0.702895 ± 15	0.513047 ± 09	0.283084 ± 12	18.53	15.52	38.07
R3-4	E	5.78	102.21	1773	0.05	0.02	0.10	0.05	0.03	0.02	0.702420 ± 11	0.513169 ± 36	0.283212 ± 13	18.12	15.45	37.58
Replicate					0.06	0.02	0.07	0.05								
R65-1	N	10.13	103.41	2074	0.03	0.03	0.08	0.05	0.02	0.01	0.702414 ± 10	0.513111 ± 09	0.283189 ± 13	18.14	15.44	37.55
R66-1	N	10.14	103.34	2600	0.07	0.04	0.11	0.16	0.06	0.01	0.702413 ± 13	0.513178 ± 11	0.283189 ± 13	18.15	15.46	37.63
R7-13	N	8.14	103.19	2020	0.05	0.06	0.08	0.05	0.04	0.01	0.702457 ± 11	0.513174 ± 10	0.283189 ± 15	18.13	15.43	37.53
R73-1	E	10.38	103.92	2547	0.04	0.02	0.07	0.06	0.03	0.01	0.702694 ± 10	0.513094 ± 07	0.283124 ± 10	18.14	15.49	37.55
R78-6	E	11.22	103.58	2450	0.15	0.02	0.21	0.04	0.14	0.01	0.702922 ± 10	0.512970 ± 09	0.283043 ± 09	19.31	15.61	39.00
R79-1	E	11.79	103.25	1620	0.11	0.05	0.19	0.05	0.10	0.01	0.702900 ± 14	-	0.283047 ± 11	19.31	15.60	39.02
R80-1	E	11.80	103.25	1619	0.19	0.06	0.29	0.11	0.18	0.01	0.702529 ± 08	-	0.283144 ± 08	18.40	15.49	37.90
R8-8	N	8.34	103.06	3180	0.06	0.06	0.08	0.08	0.04	0.02	0.702484 ± 10	0.513131 ± 10	0.283153 ± 13	18.50	15.50	37.88
R96-24	E	13.07	103.45	2577	0.06	0.03	0.10	0.11	0.05	0.0	0.702551 ± 12	0.513143 ± 07	0.283209 ± 11	18.34	15.49	37.84
R17-6	E	8.91	104.57	2715	0.13	0.02	0.20	0.07	0.10	0.03	0.702937 ± 11	0.512993 ± 08	0.283027 ± 07	-	-	-
R4-7	E	5.60	103.02	2263	0.11	0.03	0.18	0.03	0.09	0.02	0.702589 ± 10	0.513078 ± 14	0.283110 ± 09	18.49	15.49	37.97

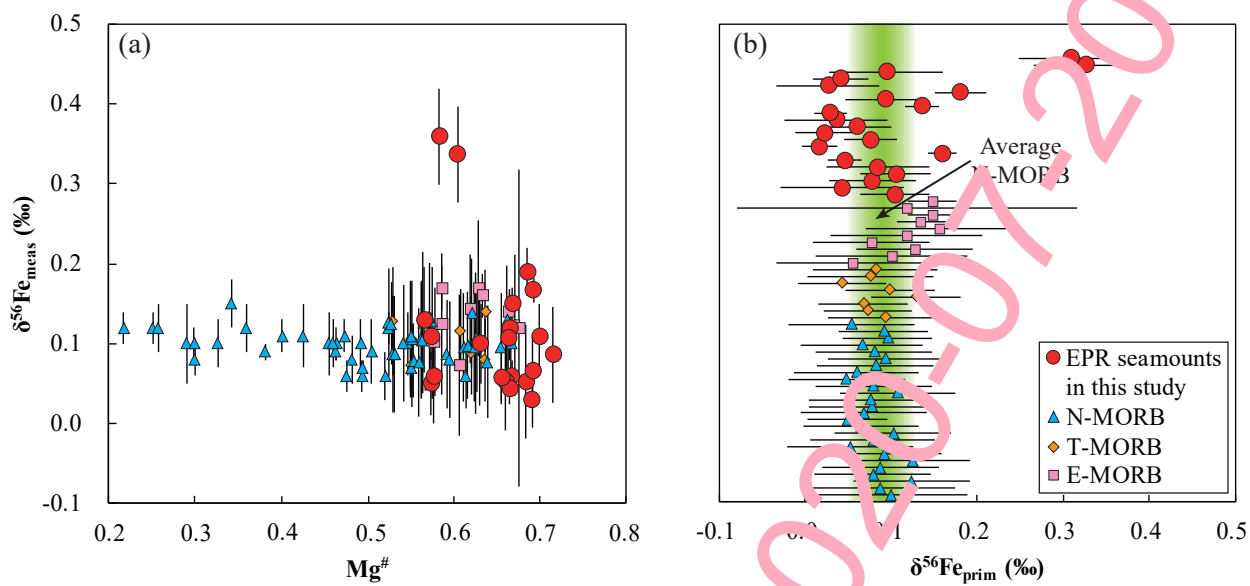
The Sr-Nd-Pb isotope data are from [Niu et al. \(2002a\)](#). The Hf isotope data are from [Zhang et al. \(2016\)](#).

Fig. 1



Accepted paper - 2020-07-20

Fig. 2



Accepted paper - 2020-07-20

Fig. 3

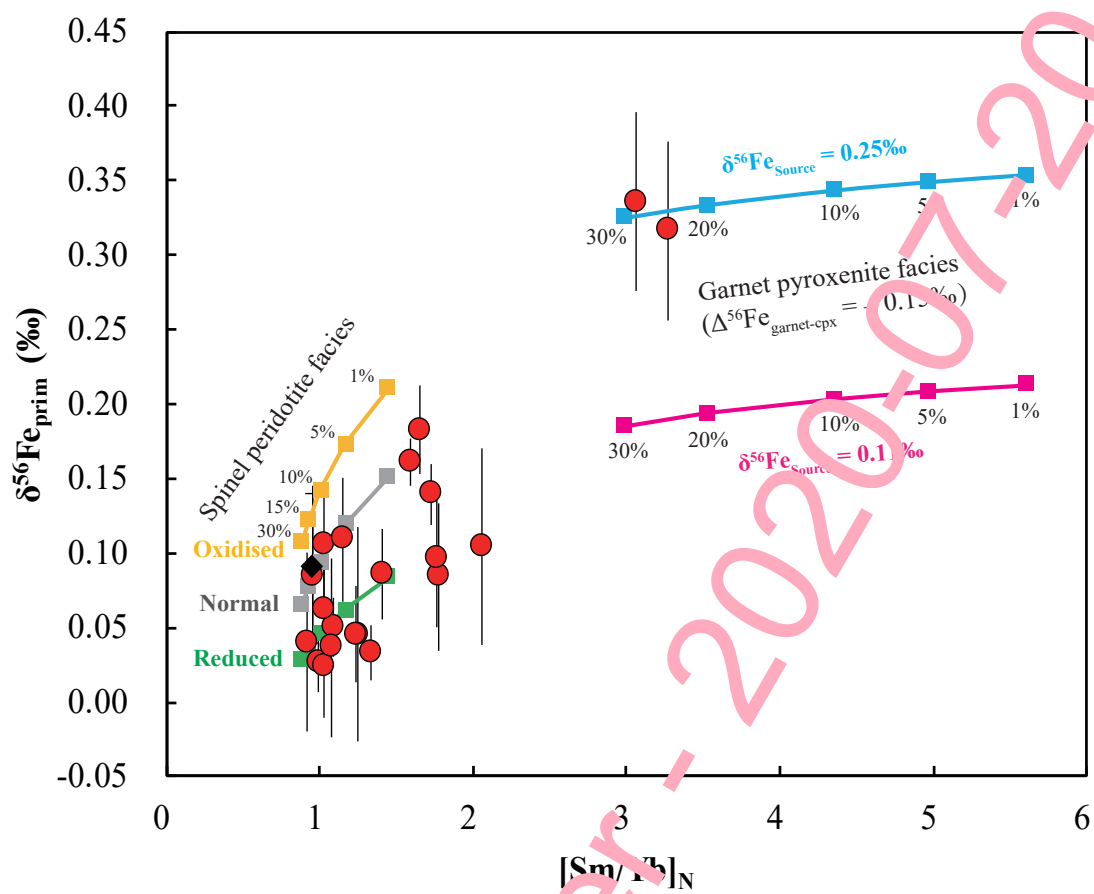
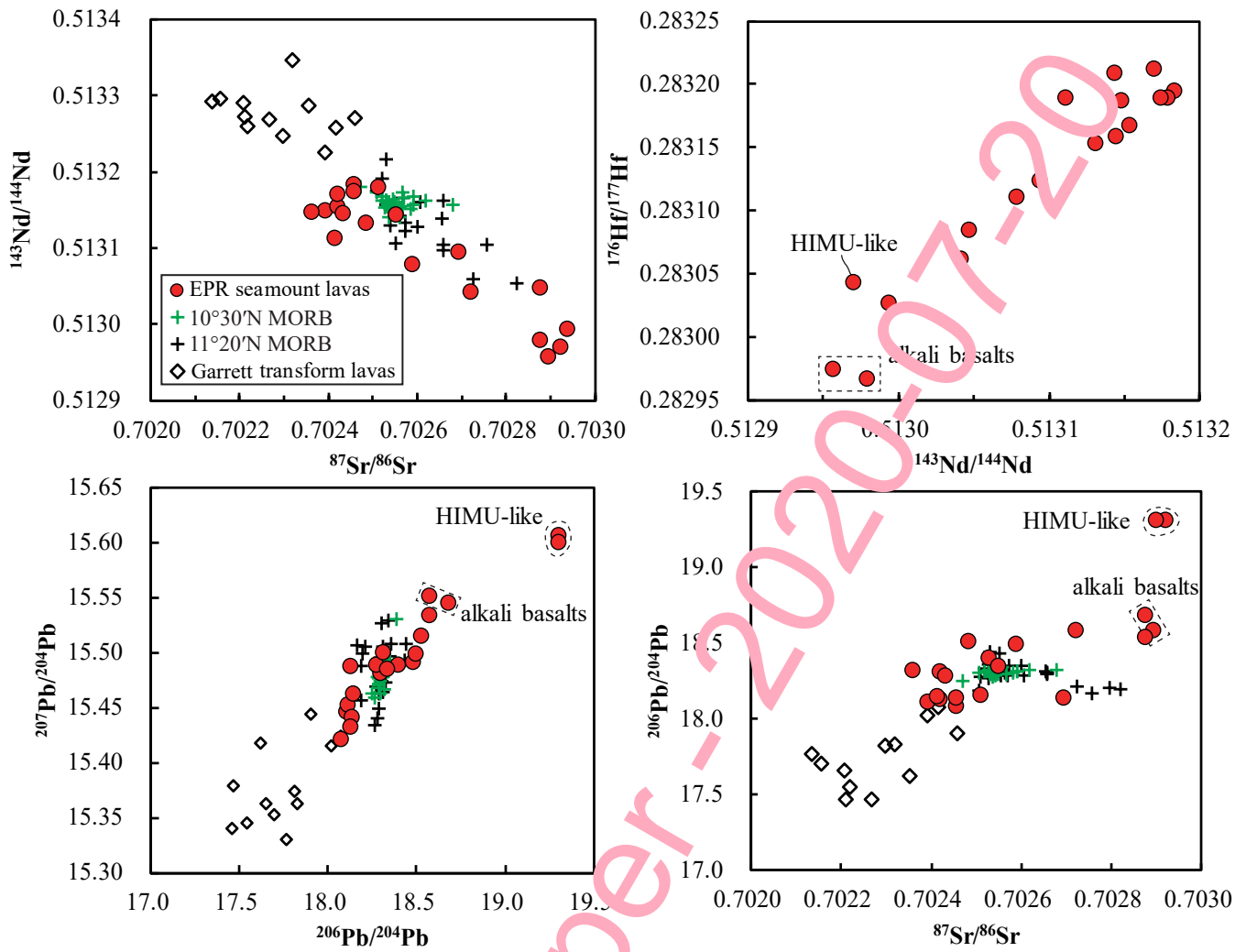


Fig. 4



Accepted paper - 2020-07-20

Fig. 5

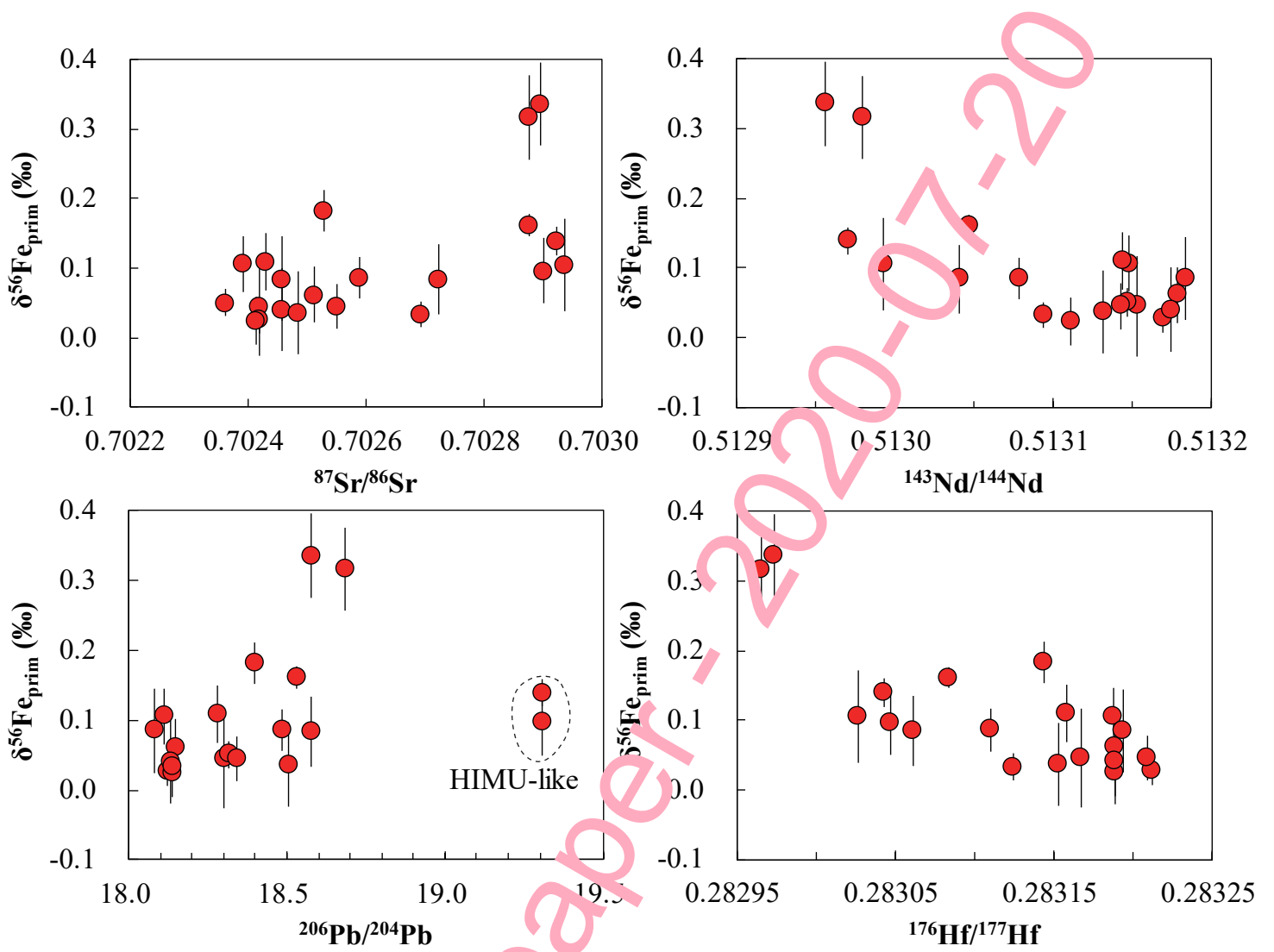


Fig. 6

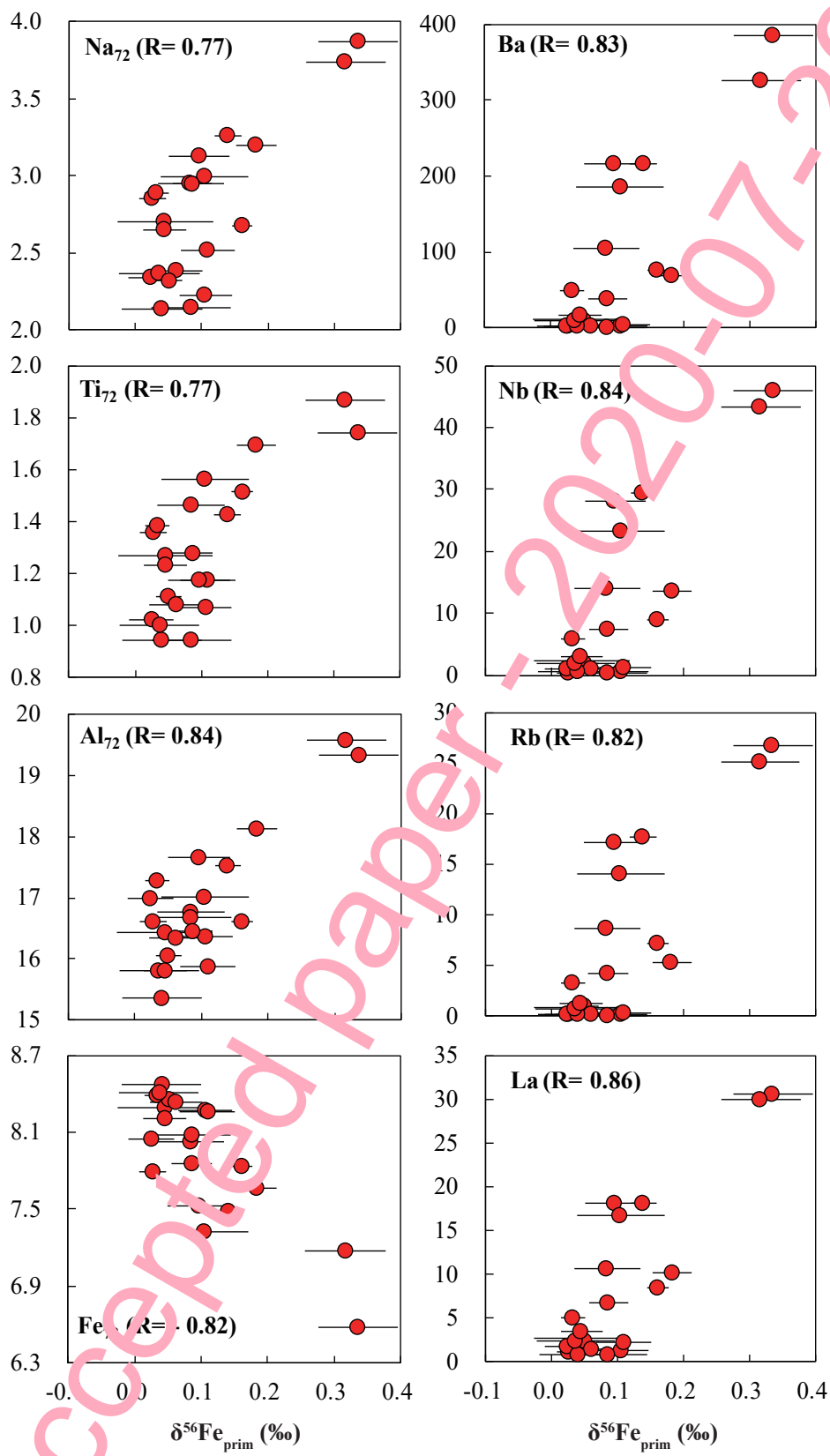


Fig. 7

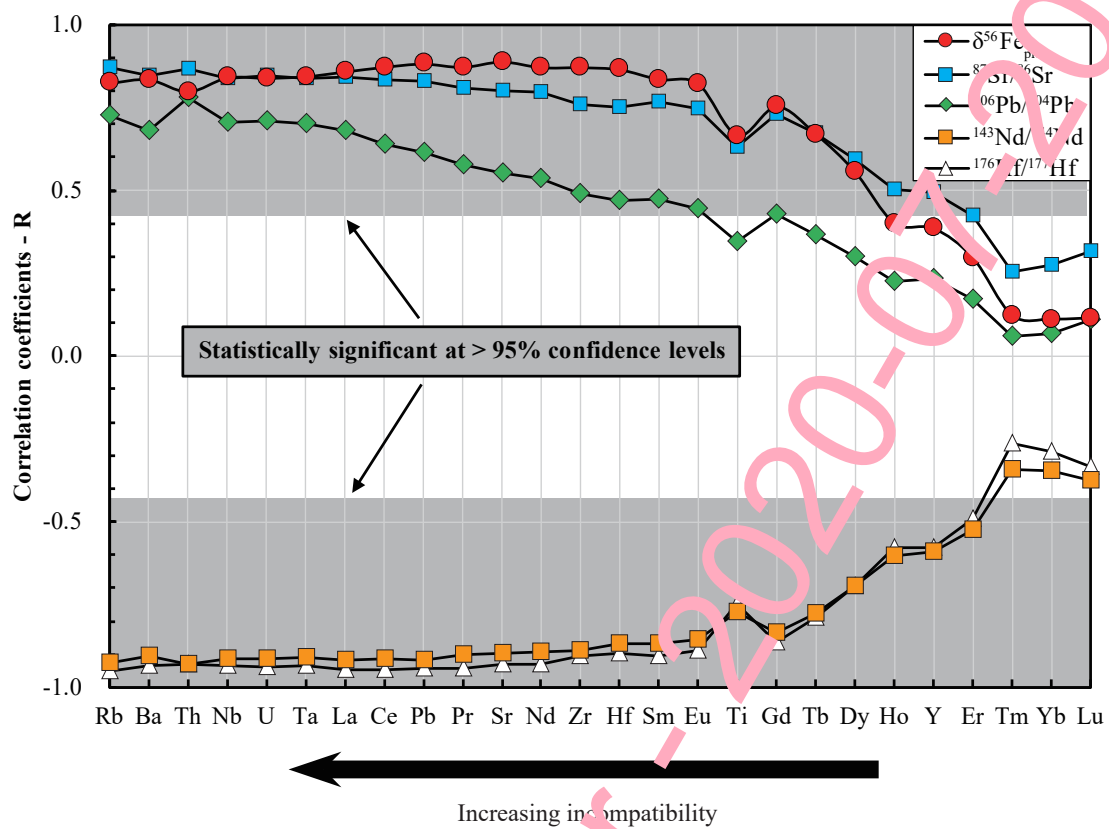


Fig. 8

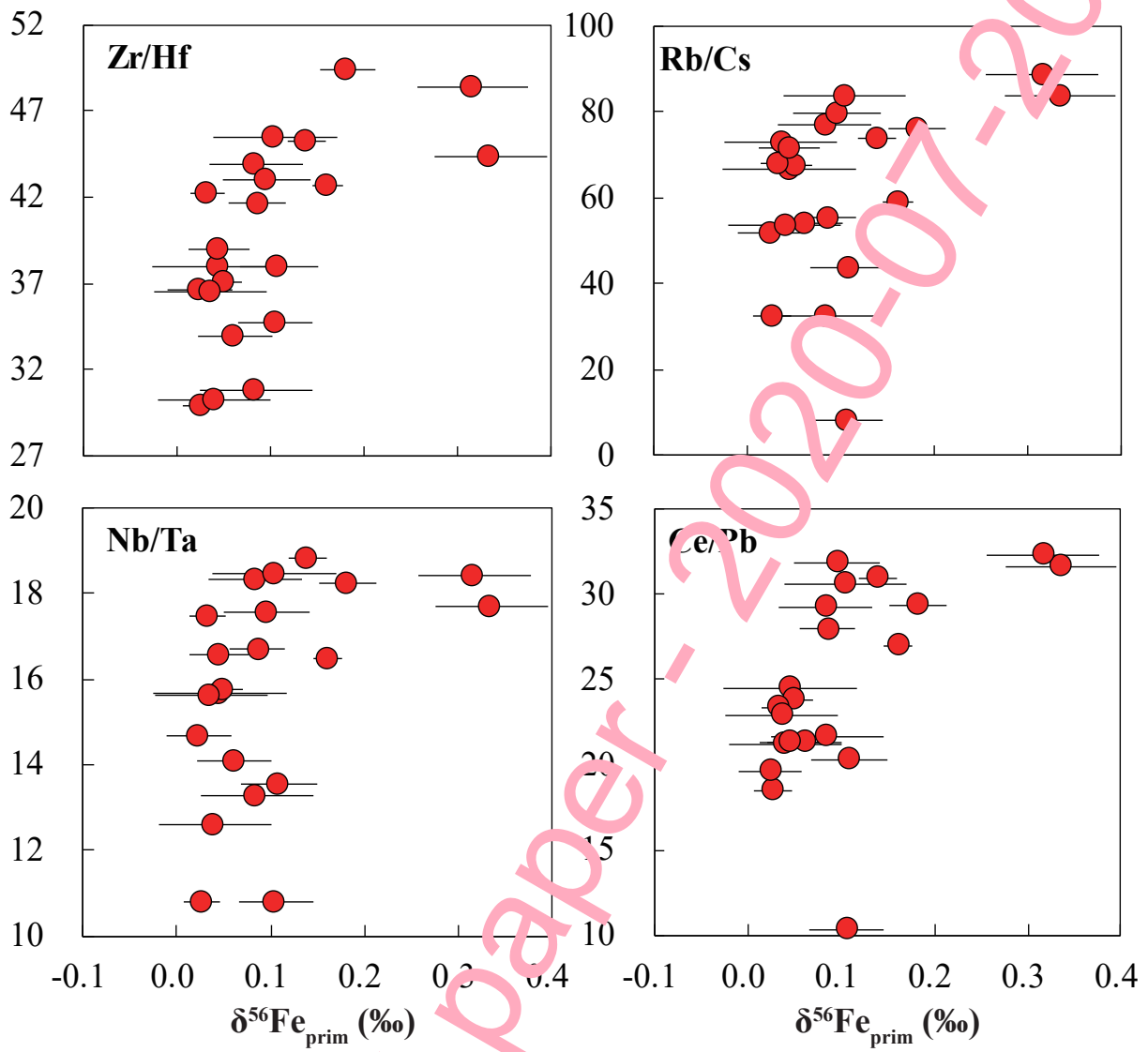
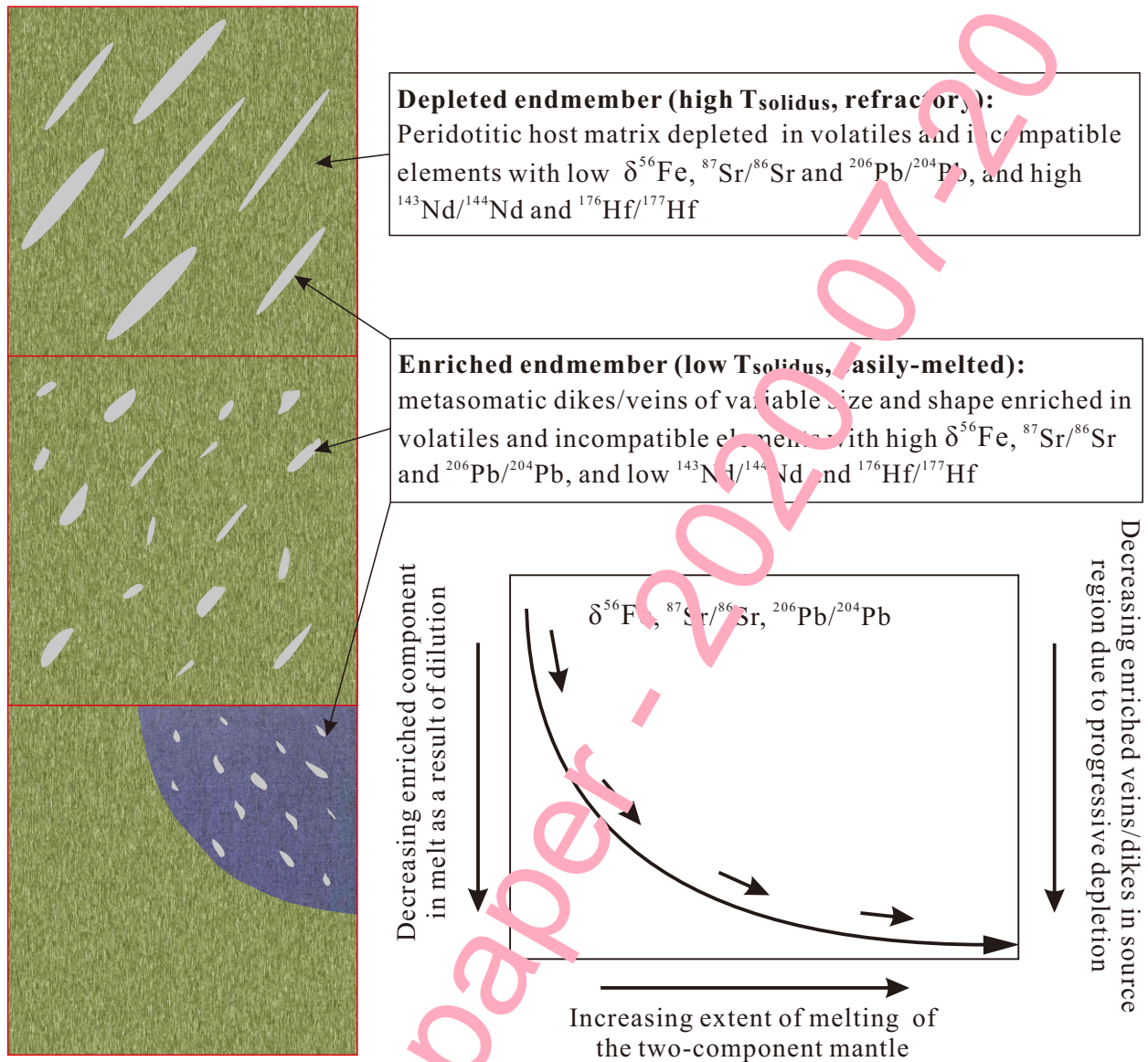


Fig. 9

(a)



(b)

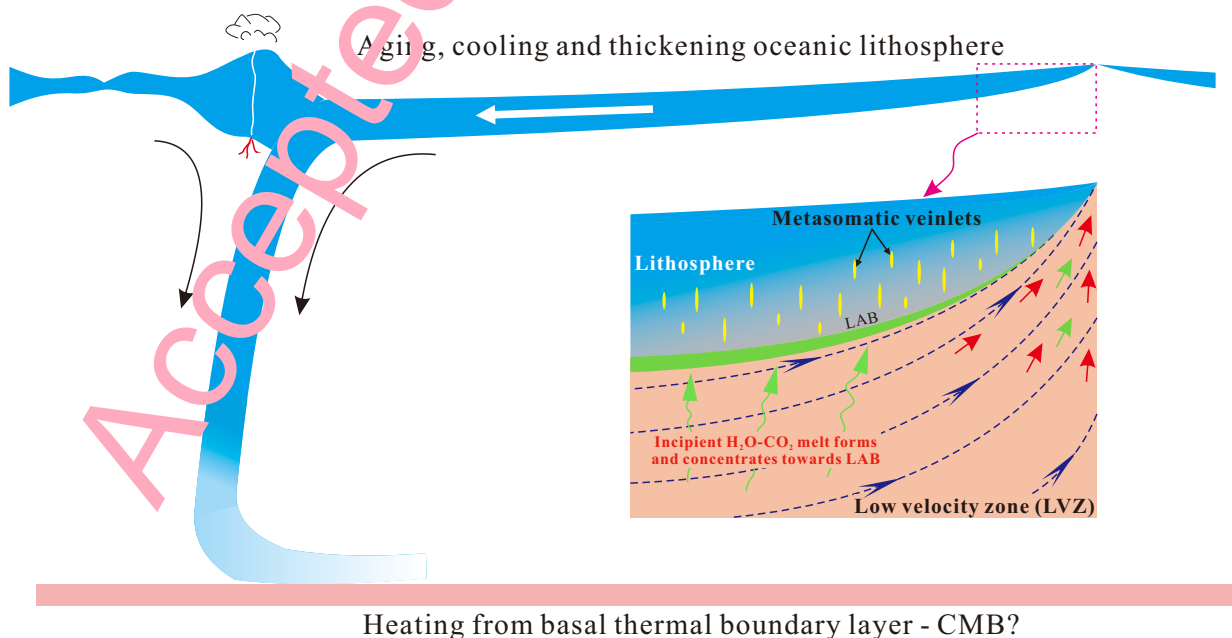
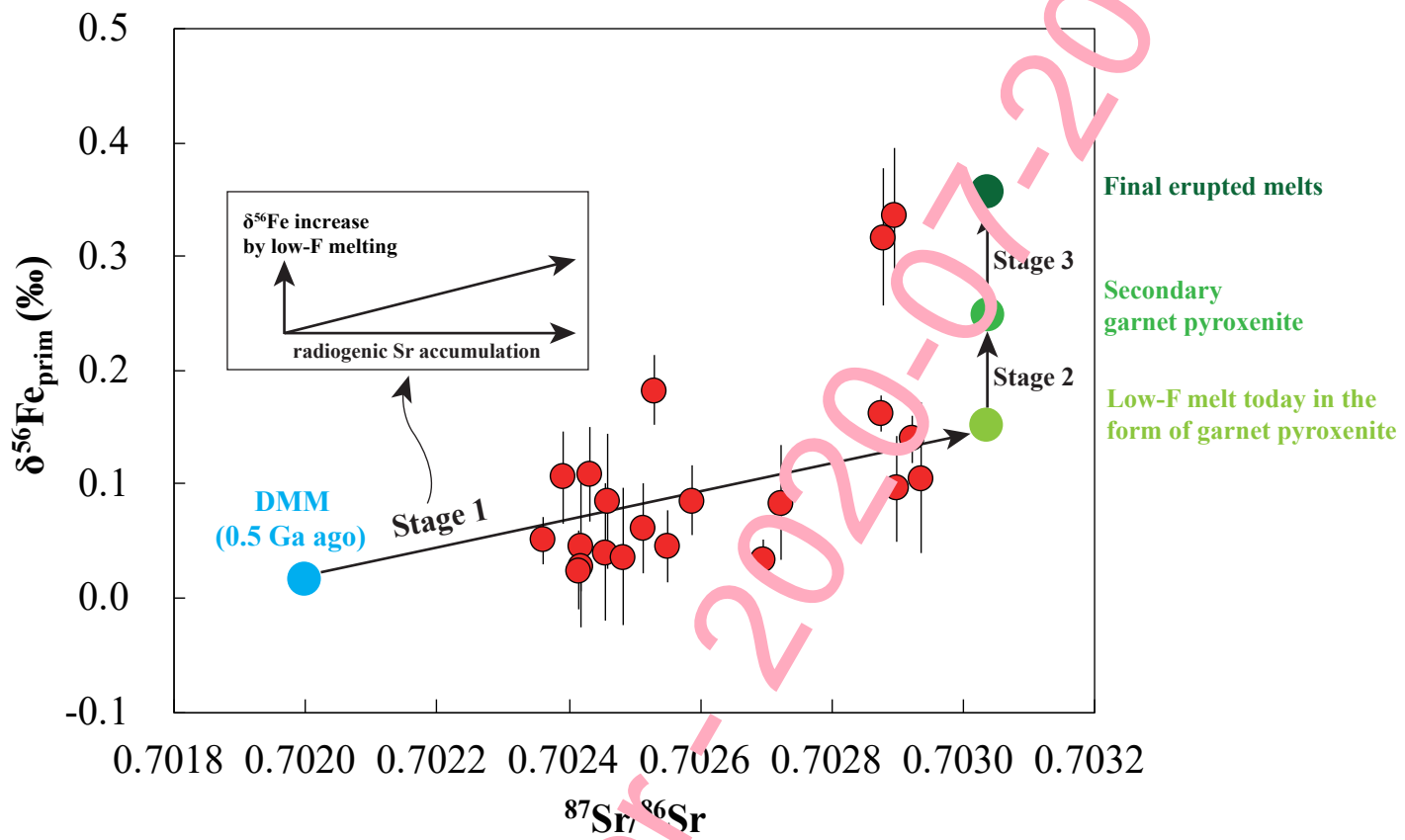


Fig. 10



Accepted paper - 2020-07-20

Accepted paper - 2020-07-20